UNIVERSITY OF CALIFORNIA, SAN DIEGO

Purkinje Cell Dendritic Spine Density From Correlated Three Dimensional Light and Electron Microscopy

A Thesis submitted in partial satisfaction of the
requirements for the degree Master of Science

in

Bioengineering

by

Lisa Lynn Fong

Committee in charge:

Professor Mark H. Ellisman, Chair
Professor Shu Chien
Professor Gabriel A. Silva

2010

The Thesis of Lisa Lynn Fong is approved, and it is acceptable in quality and form for publication on microfilm and electronically:

Chair

University of California, San Diego

2010

TABLE OF CONTENTS

LIST OF ABBREVIATIONS

DAB	diaminobenzidine
EM	electron microscopy
IVEM	intermediate voltage electron microscope
LM	light microscopy
LY	Lucifer yellow
SBFSEM	serial block face scanning electron microscopy
TEM	transmission electron microscope
UA	uranyl acetate
UHVEM	ultra high voltage electron microscope

LIST OF FIGURES

ACKNOWLEDGEMENTS

I would like to thank a number of individuals who have helped immensely with the completion of my thesis. I would like to thank Dr. Maryann Martone for her guidance and advice on all phases of the project. I would like to thank Dr. Mark Ellisman for his continued support and feedback throughout the journey. I would like to thank Dr. Erik De Schutter for his advice and several consultations. I would also like to thank several members of the lab who helped out tremendously and trained me on the techniques I used in this project, especially Eric Bushong, Naoko Yamada, Masako Terada, Andrea Thor, Monica Berlanga, James Obayashi, James Bouwer, Ohkyung Kwon, Tomas Molina, and Mason Mackey.

An adaptation of the text and figures from Chapters 1, 2, 3, and 4 will be submitted for publication with the following co-authors: Eric Bushong, Maryann Martone, Mark Ellisman, Naoko Yamada, Andrea Thor, Erik De Schutter, and Masako Terada.

ABSTRACT OF THE THESIS

Purkinje Cell Dendritic Spine Density From Correlated Three Dimensional Light and Electron Microscopy

by

Lisa Lynn Fong

Master of Science in Bioengineering

University of California, San Diego, 2010

Professor Mark H. Ellisman, Chair

Dendritic spines are primary sites of excitatory postsynaptic inputs in the CNS and changes in their number, size, and shape are linked to cognitive functions such as learning and memory. Spines influence diffusion of chemical signals along dendrites, which contributes to transmission and information processing within signal

transduction pathways. Spines have also been thought to act as a trapping mechanism to slow intracellular diffusion in dendrites. Previous studies revealed a wide range in Purkinje cell spine density, making it difficult to draw conclusions about the cell morphology of this particular neuron. Differences in spine density reported in previous studies may be due to variations in animal species, imaging method, or sample preparation. It is challenging to count spines because they fall between the resolution gaps in light microscopy (LM) and electron microscopy (EM); they are too small to resolve completely using LM and too large for EM without 3D reconstruction. In this investigation, correlated LM/EM imaging was used on identical rat Purkinje dendrites to compare spine density and address discrepancies in spine quantification at these two different microscopic scales. Dendritic segments were chosen from several areas within the dendritic tree to limit sampling bias and explore effects of dendritic segment diameter, distance from soma, and branch order on spine density estimations. Spine density was 40% lower in LM compared to EM. This is likely due to improvements in resolution in EM techniques. Additionally, little to no relationship was found between spine density and diameter, distance from soma, or branch order.

CHAPTER 1: BACKGROUND AND INTRODUCTION

1.1 Purkinje Cells and Dendritic Spines

Many neurons in the brain have dendritic spines, small protrusions extending from dendrites that are important in establishing synaptic connections (Gray, 1959a). Changes in spine number, size, and shape during development, in response to environmental stimuli, and under pathological conditions, are all linked to higher cognitive functions such as learning and memory (Bailey and Kandel, 1993; Bailey et al., 1996; Engert and Bonhoeffer, 1999; Yuste and Bonhoeffer, 2001). Spines are not distributed evenly along the length of the dendrite. Distal dendrites generally have more spines than thicker, main proximal or secondary dendrites (Figure 1.1).

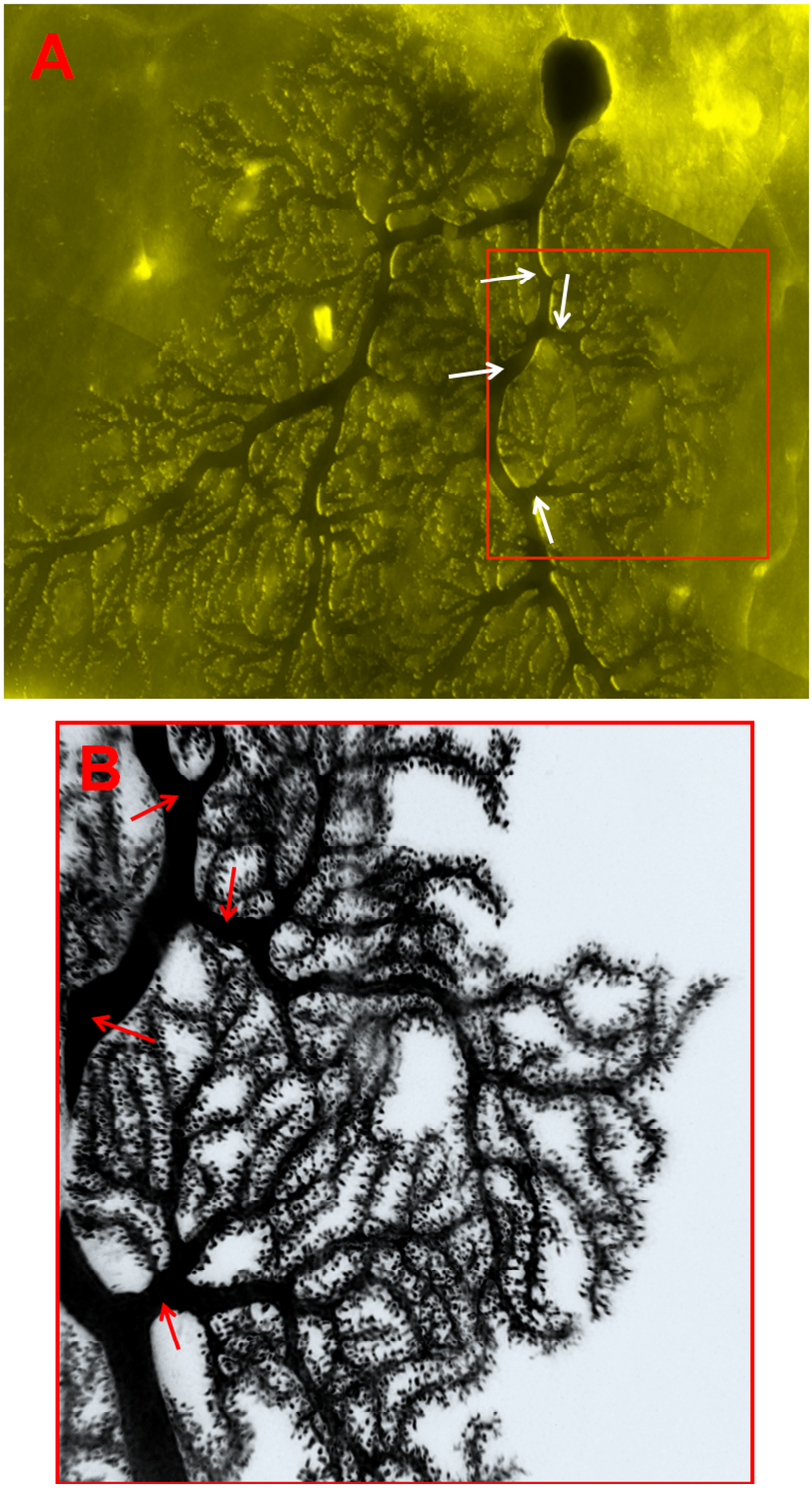

Figure 1.1: LM images of a Purkinje cell. The full (A) and zoomed-in region (B) of a Purkinje cell are shown. Thicker, main dendrites (arrows) usually appear to have fewer spines than more distal dendrites.

Purkinje cell dendritic spines are a common choice for studying synaptic plasticity since their development and connectivity have been well characterized (Palay and Chan-Palay, 1974; Chedotal and Sotelo, 1992; Morrison and Mason, 1998). Purkinje cells are large cells with a diameter of 25-40 μm and are located in a unicellular layer directly between the granule cell layer and the molecular layer of the cerebellar cortex (Figure 1.2). Purkinje cell dendritic trees are fan-shaped and lie in a single vertical plane at right angles to the longitudinal axis of the cerebellar lobule. The planes of all the Purkinje cell dendrites in a given region are parallel, so the dendritic trees stack up in a neat rank.

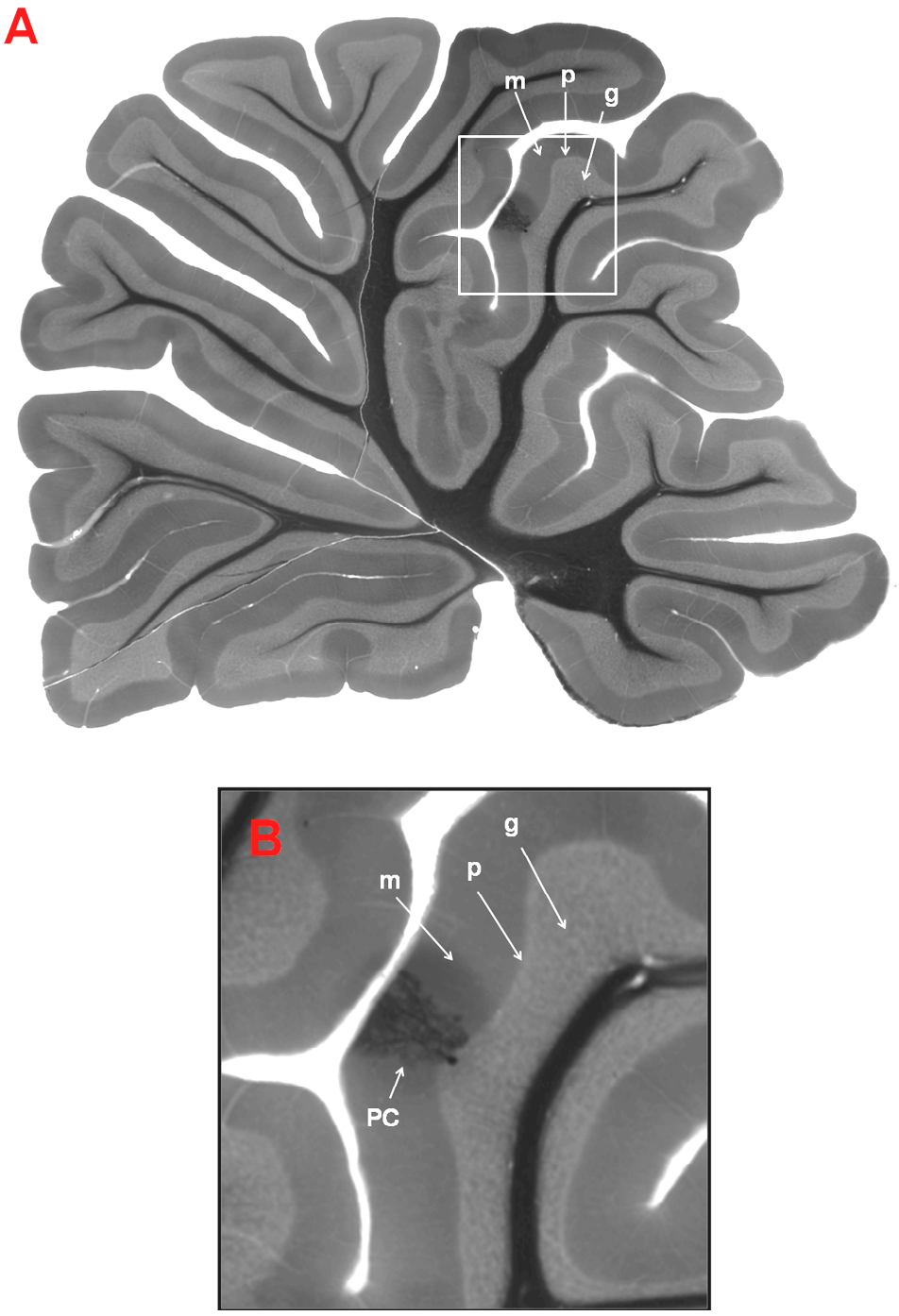

Figure 1.2: (A) Sagittal slice from the cerebellum collected on a Leica dissecting microscope at 5x magnification. (B) Zoomed-in region corresponding to the boxed area in A. Purkinje cells (PC) are located in the Purkinje cell layer (p), which is precisely in between the molecular layer (m) and the granular layer (g).

The cerebellar cortex is one of the least variable structures in the CNS with respect to its neuronal elements (Palay and Chan-Palay, 1974). The circuitry of the cerebellar cortex consists of the Purkinje cell, the sole output system of the cortex, and two inputs: 1) a monosynaptic input to the Purkinje cell, the climbing fiber, and 2) a disynaptic input, the mossy fiber-granule cell-Purkinje system.

The climbing fiber, originating from the inferior olive, branches repeatedly to "climb" along the entire Purkinje cell dendritic tree. Each Purkinje cell receives only one climbing fiber, but as many as 300 synapses can be made between a climbing fiber and its Purkinje cell (Shepherd, 2004). The synapses are made between climbing fiber varicosities, 2 µm across, and the dendritic shaft or spines of Purkinje cells. Each varicosity may synapse with 1-6 spines (Shepherd, 2004).

The second input to the cerebellar cortex is the mossy fiber, which does not synapse directly on Purkinje cells but instead synapses on granule cells. This connectivity increases the number of Purkinje cells that ultimately become stimulated by one mossy fiber axon (Shepherd, 2004). The axon of the granule cell projects into the molecular layer and splits into two branches in opposite directions, forming the shape of an uppercase "T." The fibers that form the horizontal portion of the T are precisely arrayed parallel to each other along the longitudinal axis of the lobule (Heinsen and Heinsen, 1983), and thus they are named parallel fibers. Parallel fibers cross the dendritic trees at right angles, allowing each Purkinje cell to be in a position to receive input from a large number of parallel fibers, and each parallel fiber can contact a very large number of Purkinje cells. The unique orderly arrangement of Purkinje cell dendrites and parallel fibers allows for maximum convergence and divergence in minimal space (Fox and Barnard, 1957; Fox et al., 1964, 1967; Hamori and Szentagothai, 1964).

A parallel fiber forms synapses with every 3-5 Purkinje cells it traverses. Thus, most parallel fibers passing through Purkinje cell dendritic trees won't form synapses. Still, there is such a large number of parallel fibers that each human Purkinje cell dendritic tree may be intersected by as many as 200,000 parallel fibers (Braitenberg and Atwood, 1958) and each rat Purkinje cell dendritic tree may be intersected by 175,000 parallel fibers (Napper and Harvey, 1988a), which is by far the largest number of synaptic inputs to any central neuron (Shepherd, 2004).

Spine morphology and size varies depending on cell type, but Purkinje cell dendritic spines are typically between 0.5-3.0 μm in length (Harris and Kater, 1994), with a mean length of 1.4 μm (Napper and Harvey, 1988b) and a mean volume of approximately 0.12 μm^3 (Napper and Harvey, 1988b; Harris and Stevens, 1988b), of which over 80% is the spine head (Harris and Stevens, 1988b). Purkinje cell dendrites are very dense with spines, although there is a large range in spine shape and density within the dendritic tree and across cerebellar cortical lobules (Heinsen and Heinsen, 1983). The proximal portion of the dendritic tree, innervated by a single climbing fiber, has relatively spine-free primary and secondary branches, while the distal areas are innervated largely by parallel fibers and are dense with spines, as seen in Figure 1.1.

In addition to spine shape and density differences within the dendritic tree, there is also variation in cerebellar cortical lobules. EM has shown regional differences in spine shape and density; for example, differences have been found in the neocerebellar lobule VIa and the archicerebellar lobule X (Heinsen and Heinsen, 1983). Dendritic spines in lobule VIa exhibit thin necks and large, round heads, whereas spines in lobule X show more equally sized necks and heads, where the necks are thicker and heads are thinner. The spine heads in lobule X were described

as resembling thorns or fingers as opposed to clubs in lobule VIa (Spacek and Hartmann, 1983). These regional differences indicate a possible functional significance of dendritic spines.

1.2 Importance of Spine Density

Quantifying the density of spines across individual neurons and within brain regions is important, because it provides an estimate of the number of excitatory synapses within regions that possess high densities of spiny neurons. A high synaptic density may provide key insights on how the brain is wired and on the importance of spines in learning and memory. For example the density of spines can be severely altered under environmental influences. Adult animals transferred from impoverished to complex environments showed an increase in spine density (Conner and Diamond, 1982; Lowndes and Stewart, 1994; Rollenhagen and Bischof, 1991; Rosenzweig and Bennett, 1996). When rats were trained on a spatial learning task, they showed an increase in spine density on basal dendrites of CA1 hippocampal pyramidal neurons (Moser et al., 1994). When rats were exposed to weightlessness during a 14-day space flight, spine density increased on apical dendrites in cortical layers III-IV (Belinchenko and Krasnov, 1991). These results provide evidence that dendritic complexity and spine density may be correlated with environmental complexity.

In addition to environmental influences on spine counts, the density of spines has been associated with mental agility (Zito and Murthy, 2002). Certain pathological conditions are associated with an abnormal morphology or density of spines. For example, significantly smaller dendritic arbors and lower dendritic spine density have been shown in cortical neurons of children with mental retardation (Purpura, 1975).

Spine shape and density has been studied widely in Fragile X Syndrome, the most common form of inheritable mental retardation (Hinton et. al, 1991; Irwin et. al, 2001; Wisniewski et. al, 1991). In Fragile X, dendritic spine density is increased, and spines exhibit a more immature, long, and thin form. A decrease in spine density in the neocortex and hippocampus has been shown in individuals with trisomy 21, more commonly known as Down's syndrome (Ferrer and Gullotta, 1991; Marin-Padilla, 1994; Takashima et. al, 1981; Takashima et. al, 1991). Alterations in spine morphology and number also occur in other brain disorders, such as addiction, anxiety, and depression, all of which are often associated with factors such as malnutrition, abnormal hormone levels, and chronic drug abuse (Benitez-Bribiesca et. al, 1999; Chen et. al, 2008; Robinson et. al, 2001; Shors et. al, 2001).

Along with a potential link between pathological conditions and spine density, physiological conditions reportedly also have an effect on spine density. The number of spines has also been found to decrease with age (Feldman and Dowd, 1975; Dunaevsky et al., 1999). Neurotoxins, such as lead, have been linked to impairment of brain function and a decrease in the dendritic field (Pettit and LeBoutillier, 1979). In animal models that were repeatedly exposed to psychomotor stimulants such as amphetamine and cocaine, an increase in dendritic spine density and branching was found on apical dendrites of pyramidal cells in the prefrontal cortex and on medium spiny neurons of the nucleus accumbens (Norrholm et. al, 2003; Robinson and Kolb, 1999). Additionally, spine shape and number are influenced by calcium concentration (Segal et al., 2000), hormonal state (Li et al., 2004), and epilepsy (Isokawa, 2004). Since a large proportion of excitatory axon terminals synapse onto dendritic spines, a lower spine count could signify a lower synaptic input. Taken together, these alterations in spine density may provide clues for the importance of

dendritic spines in normal behavioral and cognitive functions.

1.2.1 Biophysical Properties

Dendritic spines receive input from other neurons and compartmentalize molecules to individual synapses (Nimchinsky, et.al, 2002; Yuste and Bonhoeffer, 2004). Two-photon microscopy has shown that spines can compartmentalize calcium and thus act as biochemical compartments that isolate synaptic inputs from one another (Yuste and Denk, 1995). Activation of one synapse could lead to selective strengthening of that synapse, without influencing neighboring synapses. This synapse specificity is an important requirement for models of learning and memory (Zio and Murthy, 2002).

To study spine compartmentalization and the range of effects that spines may have on information transfer between neurons, researchers have turned to biophysical modeling of spines (Chang, 1952; Diamond et al., 1970; Rall, 1970, 1974, 1978; Carnavale and Johnston, 1982; Perkel, 1982/83; Johnston and Brown, 1983; Koch and Poggio, 1983; Kawato et al., 1984; Turner, 1984; Wilson, 1984; Coss and Perkel, 1985; Perkel and Perkel, 1985; Brown et al., 1988). Due to their small size, spines are inaccessible for direct study by electrophysiological methods (Harris and Stevens, 1988b), thus computational modeling is a useful technique for studying the theorized electrophysiological properties of spines.

Dendritic spine density is an important factor in computational modeling. Dendritic spines influence diffusion of chemical signals along dendrites, which contributes to transmission and information processing within signal transduction pathways. A recent study by Dr. Fidel Santamaria in 2006 noted that when fluorescein dextran was injected into Purkinje cell dendrites, diffusion was slower and

nonlinear in spiny portions of the distal dendrites compared to smoother proximal dendrites. The degree of anomalous diffusion was linearly related to spine density. Thus, it was hypothesized that spines cause this anomalous diffusion by acting as temporary traps for molecules moving along the length of dendrites (Santamaria et al., 2006).

Dr. Erik De Schutter and colleagues are currently using computational modeling to simulate intracellular diffusion in Purkinje dendrites to investigate possible mechanisms of anomalous diffusion. Their model used a spine density of 11-14 spines/µm, based on serial thin section EM results from Harris and Stevens (1988a). Results of De Schutter's study confirmed previous findings, showing anomalous diffusion occurs and may be due to molecular trapping by spines. However, recent studies using confocal LM have postulated a 2-3 fold lower spine density on Purkinje cell dendrites (3.15-5.15 spines/µm) (Vecellio et. al, 2000). At this density, the anomalous diffusion results cannot be accounted for by dendritic spines. De Schutter's study is one example that highlights the importance of spine density in computational modeling efforts.

1.3 Challenges in Counting Dendritic Spines in the Purkinje Cell

Dendritic spines present a challenge to quantification because they lie in the "mesoscale" dimensional range, between 5 nm^3 and 50 μm^3, which falls in the resolution gap between LM and EM. Spines are too small to be resolved by the light microscope but too large to fit on a single thin section in the electron microscope (Harris and Stevens, 1988a). As mentioned earlier, Purkinje cell dendrites are very dense with spines, and neighboring spines are often so close they may even touch one another. The necks of the spines are often thin, and it can be difficult to

distinguish one spine from another or determine which dendritic branch a particular spine is connected to. Because spine densities vary over the dendrite, spine counts are subject to sampling bias if only a limited area is sampled. It is also possible that the fluorescent dyes used for imaging at the LM level do not fill all of the spines, leading to an underestimation. Thus, the wide range in spine density from previous reports may be due to differences between imaging modalities, tissue preparation protocols (Desmond and Levy, 1988), sampling bias, and species and age differences.

1.4 Imaging Methods For Studying Dendritc Spines

Advances in LM have greatly increased resolution and made the light microscope a powerful tool, especially with the use of optical sectioning capabilities of confocal and multiphoton microscopes and computational deblurring of images. Light microscopes are widely available and require less time collecting and processing data compared to electron microscopes.

On the other hand, EM produces images with exceptional resolution and detail, far beyond what is capable on the light microscope. In the late 1950s, the electron microscope gained popularity and was used to show that the dendritic spine and the axonal bouton did in fact make a connection (Gray, 1959a and Gray, 1959b). Researchers then discovered that contractile actin was ubiquitous in dendritic spines, which led to studies on spine motility and its role in learning and memory (Blomberg et al., 1977; Crick, 1982; Fifkova and Delay, 1982; Matus et al., 1982).

However, there are still many drawbacks to EM that make it less optimal for many researchers compared to LM. Although the electron microscope can achieve high resolution and fine detail, there are limits to the size of the tissue sample that

can be imaged. Individual thin sections prepared for conventional transmission EM are so thin that they rarely can capture an entire cellular structure. Conventional TEMs use sections of about 60-80 nm in thickness, and most cellular structures are much larger than this, so it is challenging to obtain accurate information about the structures from such thin sections. In conventional transmission electron microscopy, 3D structures are often inferred from a series of 2D images, causing features to be superimposed and sometimes challenging to interpret (Frey et al., 2006). In comparison to EM, LM allows a much larger view of a tissue sample.

Another drawback to EM is a sampling bias. Due to the limits in the size of the tissue sample that can be imaged, combined with the large time requirements, a small number of samples is often collected. Researchers sometimes select areas within the tissue based on various criteria, such as the quality of structural detail seen in the viewing screen. Thus, selection is not always random.

There have been recent advances in EM, especially in high voltage electron microscopes, which have an accelerating voltage of 400 KeV-3 MeV, compared to 40-200 KeV in the traditional TEMs (Martone et al., 2000). The accelerating voltages of conventional TEMs are not powerful enough to allow electrons to penetrate tissue sections much thicker than 200 nm (Martone et al., 2000). When thicker sections are used, there is a loss of electron energy as a result of interactions of the electrons in the specimen, causing a loss in resolution (Martone et al., 2000). High voltage electron microscopes allow thicker sections to be used, as the higher accelerating voltage increases the mean-free electron path and enables electrons to penetrate through the thicker sample without losing electron energy and compromising image quality. Through the use of thicker sections, fewer sections need to be collected in order to fully capture the structure of interest.

In recent years, electron tomography has become a powerful technique to study 3D structure and provide a much more realistic image of the structure of interest. Electron tomography utilizes a series of projections through the structure collected at different angles to produce a 3D reconstruction with nanometer resolution (3-8 nm; Frey et al., 2006). The specimen is tilted around a fixed axis perpendicular to the electron beam, and projections are recorded at one- or two-degree angular increments from +/- 60º to 80º (Frey et al., 2006). 3D reconstruction is based on the mathematical principles of the Radon transform, using a backprojection of tilt images to fill a 3D density map (Frey et al., 2006). Once the raw data from the tilt series is collected, these projection images must be aligned, and the 3D density map can then be computed, usually by a weighted backprojection algorithm (Baumeister, 2005). The resulting 3D reconstruction can be rendered and viewed as a series of 2D slices computed through the volume or as a 3D volume.

Although electron tomography is useful for obtaining 3D information and provides sufficient resolution for studying small structures such as dendritic spines, it is labor intensive and time consuming. A considerable amount of time must be spent collecting data and reconstructing volumes. Additionally, it is not possible to acquire larger 3D reconstructions covering tens or hundreds of micrometers with electron tomography. For these reasons, serial block face scanning electron microscopy (SBFSEM) is becoming more widely used. SBFSEM is an automated technique that is a scanning electron microscope with a built in ultramicrotome (3View). SBFSEM collects volume information by imaging sections before they are removed from the block face. A focused beam of electrons is raster-scanned over the tissue, and the block face is repeatedly imaged. Imaging the entire block face is advantageous because it eliminates the need to manually handle ribbons of fragile sections used in

TEMs. The lateral resolution is not as good as that of a TEM, but it is still sufficient to manually trace neuronal processes. Additionally, a large amount of time is reduced in collecting the data and reconstructing the volume (Denk and Horstmann, 2004).

1.5 Previous Studies of Purkinje Cell Dendritic Spine Density

Many efforts have been made to determine dendritic spine density in Purkinje cells. The findings have varied significantly, making it difficult to draw any conclusions. Many spines are large enough to detect in the light microscope. LM may be the appropriate method for spine analysis by many researchers. For one, LM is compatible with live imaging. LM allows researchers to look at a larger field of view. Additionally, fewer laboratories have electron microscopes, and light microscopes are more readily available.

Even with the advanced capabilities of the light microscope, spine counts have varied using this technique. Spine densities as low as one spine/μm (Tavares et al., 1983), all the way to 7.65 spines/μm (Pysh and Weiss, 1979), have been found in Purkinje cells using LM. Many researchers agree that LM likely underestimates the number of spines (Heinsen and Heinsen, 1983; Fox et al., 1957). Spines projecting in front and behind the dendritic shaft may be obscured by the shaft or by neighboring spines. LM, including confocal LM, has particularly poor z resolution. With a high numerical aperture lens, the diffraction limited xy resolution is about 0.2 μm, but the z resolution is closer to 0.8 μm. Due to limits in resolution, spine necks may be difficult to see, making it challenging to follow a spine back to its parent dendrite.

Increased resolution and structural detail in the electron microscope leads one to believe it is the obvious choice in obtaining accurate spine counts. However, a range of spine densities for the Purkinje cell has been found using EM techniques,

from 2.35 spines/µm (Lee et al, 2007) to 17 spines/µm (Napper and Harvey, 1988b). Purkinje cell spine densities from the literature are reported below in Figure 1.3. As mentioned previously, differences in tissue preparation protocols (Desmond and Levy, 1988), sampling bias, and species and age variations could all play a role in this large range of spine density values. Clearly a more controlled study is necessary to fully evaluate dendritic spine density in the Purkinje cell.

LM Spine Density	Animal Species & Age	Reference
1.00 spine/µm	rat, 8 weeks	Tavares et al., 1983
1.5 spines/µm	monkey, adult	Fox and Barnard, 1957
3-5 spines/µm	mouse, 78-204 days	Vecellio et al., 2000
7.65 spines/µm	mouse, 35 days	Pysh and Weiss, 1979

EM Spine Density	Animal Species & Age	Reference
2.35 spines/µm	rat, 2-3 months	Lee et al, 2007
5.15 spines/µm	rat, adult	Hillman and Chen, 1984
7.00 spines/µm	mouse, young adult	Spacek and Hartman, 1983
11.60-14.30 spines/µm	rat, adult	Harris and Stevens, 1988
17.00 spines/µm	rat, young adult	Napper and Harvey, 1988

Figure 1.3: Comparison of Purkinje cell spine densities reported in the literature. There is a wide range found in both LM and EM techniques, indicating a need for a more controlled study.

1.6 Objectives

Advances in both LM and EM and associated computer technologies have bridged the gap that traditionally existed in terms of resolution and scale and has improved 3D analysis in both techniques (Martone et al., 2000). However, the literature has shown a large variability in spine density in the Purkinje cell. The challenge is that each study has its own set of variables—imaging technique, animal

type and age, and sample preparation methods are likely to differ among previous studies. To minimize these variables as much as possible, we used three dimensional correlated LM and EM. Correlated microscopy allows the same dendritic segment and its spines to be imaged with both the light and electron microscopes to better evaluate discrepancies in spine quantification.

Additionally, three different EM techniques were used: a JEOL 4000 intermediate voltage electron microscope (IVEM) for serial section tomography, a Hitachi H-3000 3 MeV ultra high voltage electron microscope (UHVEM) in Osaka, Japan for thick section tomography, and an FEI Quanta FEG 200 VPSEM equipped with a Gatan 3View system for serial block face scanning electron microscopy (SBFSEM). Each of these imaging techniques has their own advantages as discussed previously in Section 1.4, and they were used to compare spine density values across EM imaging methods.

Using correlated LM and EM, the following questions were addressed in this investigation:

1. *Spine density with variable imaging methods*: Is there a difference in spine density when the identical dendritic segment is evaluated using both LM and EM? Researchers typically agree that LM underestimates spine density.
2. *Spine density with variable location among the neuron*: Does spine density vary as branch order or distance from the soma increases?
3. *Spine density with variable dendritic shaft thickness*: How does spine density change with variations in dendritic shaft diameter? Does an increase in diameter, and hence an increase in surface area of the dendritic segment, show an increase in the number of spines?

An adaptation of the text and figures from Chapters 1, 2, 3, and 4 will be submitted for publication with the following co-authors: Eric Bushong, Maryann Martone, Mark Ellisman, Naoko Yamada, Andrea Thor, Erik De Schutter, and Masako Terada. The thesis author was the primary contributor to the work of this chapter.

CHAPTER 2: METHODS AND MATERIALS

2.1 Sample Preparation For LM (Fixation Of Brain Tissue)

Three young adult (1 month old) male Sprague-Dawley rats were anesthetized with Nembutal and perfused with Ringers solution at 37℃ containing xylocaine and heparin for 2 minutes, followed by 4% PFA in PBS for 10 minutes. The brain was removed and placed in 4% PFA on ice for 1-2 hours. The cerebellum was cut sagittally into 100 μm thick slices on a Leica VT1000S vibratome and slices were stored in PBS on ice.

In each animal, two Purkinje cells were successfully filled in two separate slices with aqueous 5% Lucifer Yellow (LY) dye. Each neuron was impaled and the dye was injected by applying a 0.5 second negative current pulse (1 Hz) until the cell completely filled with dye. The slices were then post-fixed in 4% PFA in PBS on ice for approximately 30 minutes. The sequence of steps involved in this investigation is presented in Figure 2.1 below.

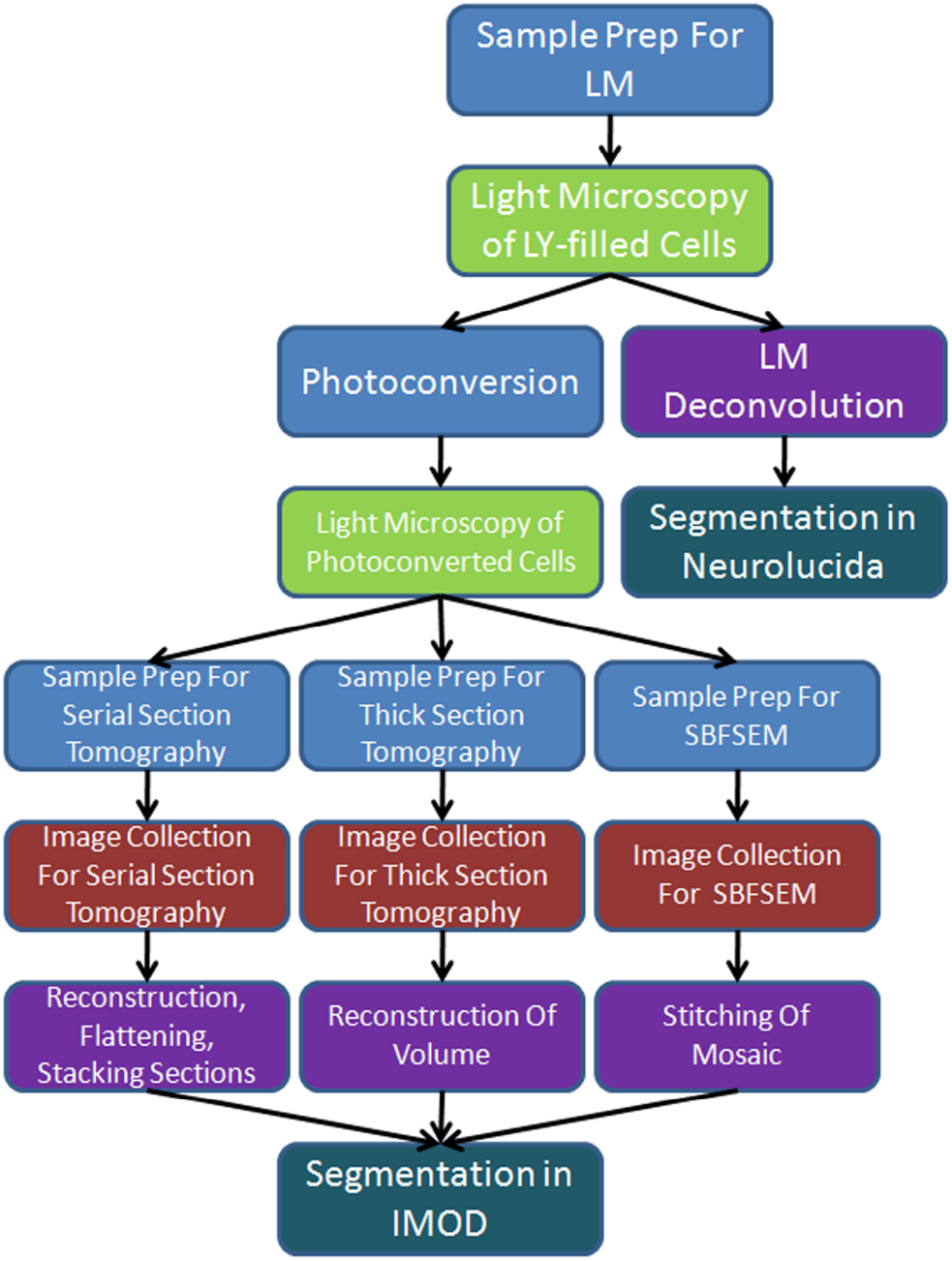

Figure 2.1: Flow chart of each step involved in the correlated LM and EM study.

2.2 Light Microscopy

Following cell filling, a z-series of images was collected for each whole fluorescent cell on an Olympus FluoView 1000, a single photon confocal microscope. These volumes were collected for determining the dendritic distance from the soma and branch order of chosen dendritic segments. The volumes were also used for mapping purposes. A #1.5 Mat-tek dish was used, and water was used as both the immersion and mounting media. A 20x air objective with a 0.75 numerical aperture was used. The step size for the low resolution volumes was either 2 µm or 3 µm, and the XY spacing was 0.258 µm or 0.414 µm, respectively.

Next, an area of the dendritic tree was selected for the correlated study. It was chosen by identifying a region where dendrites and spines were successfully filled with LY dye. The slices were imaged on the Olympus FluoView 1000 with 440 nm excitation and 500-600 nm emission. The slices were imaged in PBS in a #1.5 Mat-tek dish using a 1.20 numerical aperture 60x water objective. The step size for high-quality deconvolution compatible volumes was either 0.2 µm or 0.3 µm, and the XY spacing was 0.09 µm or 0.082 µm, respectively.

2.3 Photoconversion

Following LM imaging, the slices were post-fixed in 2% glutaraldehyde in PBS for 10 minutes, to prevent leakage of the LY dye and achieve strong ultrastructural preservation of the tissue. The tissue was then incubated in PBS/glycine for 10 minutes, in order to prevent polymerization of diaminobenzidine (DAB) by glutaraldehyde.

For photoconversion, the slices were placed in PBS containing 1.5 mg/mL DAB and 1 mg/mL potassium cyanide. The slices were allowed to sit in solution on a

cold stage for about two minutes. A nylon mesh was used to hold down the slices in a #0 Mat-tek dish. Oxygen was blown onto the surface during the photoconversion. The sample was illuminated using a Lucifer Yellow filter cube. When the fluorescence was extinguished and the cell turned distinctly brown, the illumination was ended.

2.4 LM Survey Images of Photoconverted Cells

Survey images were collected to follow the area of interest back to its location within the cerebellum and to locate the corresponding portion later in the electron microscope. Low magnification images of each entire cerebellar slice were acquired on a Leica MZFL III fluorescent dissecting microscope to show the location of the photoconverted cell within the cerebellum. Additionally, an Olympus DSU equipped with a 20x objective was used to collect images of each full photoconverted cell to see its location between the molecular layer and the granular layer. Through focus series were collected, and the series were later combined using Combine ZM, a freely available image processing software package used to produce a combined image with a high depth of field (Alan Hadley, United Kingdom; http://www.hadleyweb.pwp.blueyonder.co.uk/CZM/combinezm.htm).

For Animals 1 and 2, 3D mosaics of the full photoconverted cells were acquired on a FluoView 1000 using a 60x oil objective. The cells were imaged with a zoom of 2x and Kalman of 3. The voxel dimensions were (0.103 x 0.103 x 1.0) µm. These mosaics were processed using ImageJ plugins developed by Chow et al., (2006). The first part of the processing procedure is normalization, to correct for shading artifacts on each individual image, as a result of the optical characteristics of the microscope. Normalization is necessary to eliminate any border regions of each

image and to improve accuracy of alignment. The next part of the ImageJ plugin aligns the individual images to ensure registration of individual features and a seamless transition between images.

2.5 Sample Preparation For Tomography (Dehydration, Infiltration, and Embedding)

Following photoconversion, slices for serial section tomography and thick section tomography were post-fixed in 0.5% OsO4 in PBS for 30 minutes. For the dehydration phase, they were washed for 10 minutes each in a graded alcohol series of ice-cold 70%, 80%, 90%, 100%, and 100% EtOH. Next, they were placed in ice-cold dry acetone at room temperature for 10 minutes, followed by room temperature dry acetone for 10 minutes.

Following dehydration, the slices were infiltrated overnight for about 12 hours in a solution of equal parts of Durcupan ACM resin and acetone with agitation. The next day, slices were placed in a 2:1 solution of Durcupan ACM to acetone for about 5 hours with agitation. The slices were then transferred to vials containing 100% Durcupan ACM for overnight incubation with agitation. The following day, the slices were placed in fresh 100% Durcupan ACM for 5 hours with agitation. The slices were then flat embedded between mould-release coated slides in fresh 100% Durcupan ACM and placed into a 60° oven for 72 hours to be po lymerized. The glass coverslip was removed from the bottom using a razor blade, and the photoconverted area was cut out and glued to a block for sectioning.

2.6 Sample Preparation for SBFSEM

Following photoconversion, one slice was prepared for SBFSEM. The slice was washed in cacodylate buffer containing 2 mM $CaCl_2$ for 30 minutes. It was then covered in equal volumes of 3% potassium ferrocyanide solution and 4% OsO_4 for 1 hour and agitated periodically. Meanwhile, 0.1 g thiocarbohydrazide was added in 10 mL ddH_2O and heated in a 60º oven for 1 hour, shaking occasionally. The slice was washed with room temperature ddH_2O and placed in the filtered thiocarbohydrazide solution at room temperature for 20 minutes. The slice was washed with room temperature ddH_2O and placed in 2% OsO_4 in ddH_2O for 30 minutes at room temperature. Next, the slice was washed with room temperature ddH_2O, placed in 2% aqueous uranyl acetate (UA), and left in the refrigerator overnight.

The next day, 0.066 g of lead nitrate was dissolved in 10 mL aspartic acid solution and adjusted to a pH of 5.5 with 1 N KOH. After this was accomplished, the solution was heated in a 60º oven for 30 minutes. Care was taken so that no precipitate formed. The slice was washed with ddH_2O, placed in the lead aspartate solution, and left in the oven for 30 minutes. The slice was then washed in room temperature ddH_2O and dehydrated using a graded ethanol series of ice-cold 70%, 90%, 100%, and 100% EtOH for 10 minutes each. The slice was placed in ice-cold acetone and left at room temperature for 10 minutes, followed by room temperature acetone for 10 minutes.

Following dehydration, the slice was infiltrated in Durcupan. The slice was placed in a solution of 25% Durcupan ACM to acetone for a few hours with agitation, followed by a 50% Durcupan ACM to acetone solution overnight with agitation. The next day, the slice was placed in a 75% Durcupan ACM to acetone solution for a few hours with agitation, followed by 100% Durcupan ACM overnight with agitation. The

next day, the slice was placed in fresh 100% Durcupan ACM for a few hours with agitation. The slice was then mounted on a glass slide and placed in a 60º oven for two days to allow for polymerization.

2.7 Serial Section Electron Tomography Image Acquisition

For serial section tomography, serial sections from the Durcupan-embedded tissue were cut at a thickness of 0.5 µm. These semi-thick serial sections were collected on Luxel grids (Ted Pella), which fit 10-15 sections per grid. The sections were stained and stabilized with 2% aqueous UA for 30 minutes and Sato lead for 12 minutes. The slices were then carbon coated to further help stabilize the tissue and reduce drift from occurring in the microscope. 20 nm colloidal gold particles were placed on both sides of each grid, serving as fiducial markers for alignment of the tilt series.

Serial section tomography was performed using a JEOL 4000EX IVEM with a 4k x 4k camera at an accelerating voltage of 400 KeV. The magnification was set to 4000x, and the beam current was about 125 µA.

2.7.1 Selecting the Dendrite

Criteria for selecting a dendrite for correlated analysis were: 1) the dendrite was fully contained in the ribbon prepared for EM (including axial spines) and fully captured in the fluorescent z-stack collected on the light microscope, to ensure that the exact same dendrite segment was collected on both microscopes; 2) dendrites with a range of diameters were selected, as spine density may be a function of dendrite diameter (Roth and Hausser, 2001) and conversely, dendrite diameter may impact the ability to detect spines using different modalities; 3) dendritic segments

were chosen with varying distances from the cell body to include both distal dendrites and proximal dendrites with a lower branch order; 4) only dendritic segments that were between branch points were chosen, because branch points may interfere with accurate spine counts; 5) dendritic segments near a blood vessel or other obvious structures were selected to make it easier to follow the same dendritic segment in subsequent sections; 6) the dendrite of interest needed to be centered within the ribbon section on the Luxel grid to avoid being cut out of view at high tilt angles. If a dendrite segment met all of the above criteria, it was chosen for tilt series acquisition.

2.7.2 Tilt Series Acquisition

A total of 9 dendritic segments were collected with serial section tomography, and each dataset required approximately 10 tilt series. To prepare for tilt series collection, the real time video camera was used to display the ROI, and features such as the dendritic shaft, spines, and gold particles were outlined on the computer monitor with a marker. When a tilt angle was changed, these features were used as guides to move the stage appropriately back to its original spot defined by the marker outlines if necessary, since eucentricity was not perfect and slight movement of the stage occurred periodically. This ensured that the tilt series was kept centered on the ROI during image acquisition. When the ROI was centered at each tilt angle, the current density was set to about 20 Pa/cm^2, and the X and Y wobblers were used to bring the image into focus.

For tilt series collection, the tilt angle was set at –60°, and an image was shot every two degrees until a tilt angle of +60° was reached, for a total of 62 images for every tilt series. Images at each tilt angle were recorded and saved as an image stack with the SerialEM software (University of Colorado, Boulder).

2.7.3 Tomographic Alignment and Reconstruction

Following tilt series collection, the raw image volumes were processed using the IMOD (Kremer et al., 1996), version 3.13.5, and TxBR (Transform-Based Back Projection; Lawrence et al., 2006) software tool suites. The volumes were cropped to eliminate any artifacts due to the CCD camera. The colloidal gold particles were used to refine the tilt angles, image shifts and rotations, magnification changes, and beam and sample distortions. These refinements were then applied to the tilt series image stack to produce an aligned stack.

Following alignment, 3D reconstruction was performed. This was accomplished using the image densities in the aligned image stack. R*-weighted backprojection was applied using TxBR. The resulting image is shown in Figure 2.2.

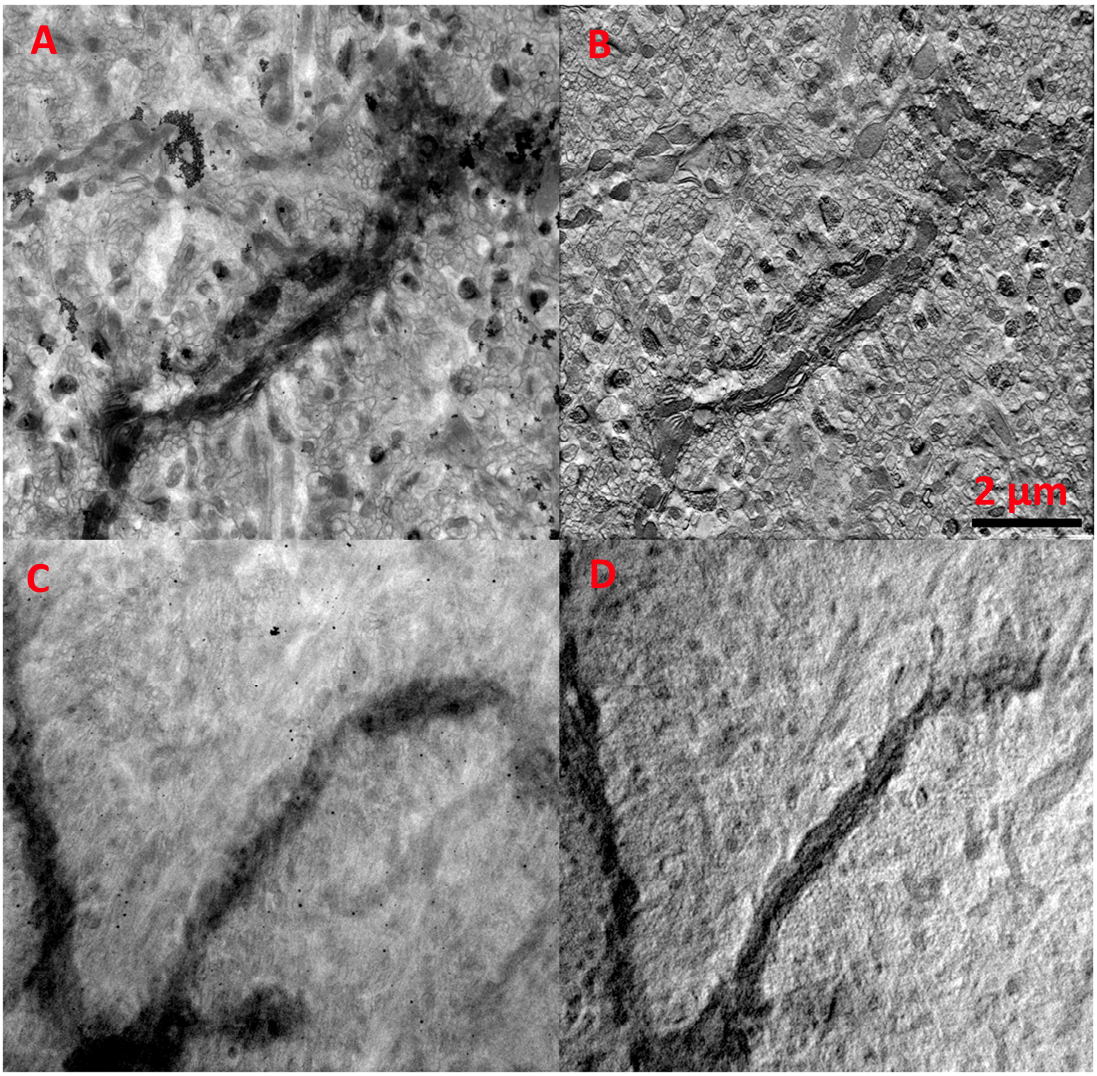

Figure 2.2: Raw versus reconstructed slices from serial section tomography and thick section tomography. (A) Single slice from a tilt series on collected on the JEOL 4000 at 4000x magnification. (B) Computed slice through the volume after backprojection and reconstruction. (C) Single slice from a thick section tomography collected on the Hitachi H-3000 3 MeV UHVEM at 5000x magnification. (D) Corresponding computed slice through the volume after backprojection and reconstruction.

2.7.4 Flattening To Reduce Warping

After reconstructing the volume, a flattening procedure was used to remove the out-of-focus areas and reduce any warping that occurred during tilt series acquisition. First, a model file was created in IMOD to fully characterize the specimen boundaries. To accomplish this, the TxBR reconstruction of the warped volume was

loaded into IMOD. The out-of-focus areas were manually traced, and this was repeated for both the bottom and top slices of the volume. An accurate boundary model file is crucial for de-warping the volume. Upon completion of the flattened models, a TxBR flattening script was used to create a flattened version of the reconstructed volume.

2.7.5 Stacking Serial Sections

Following the flattening routine, the serial sections were ready to be stacked into the full volume. Stacking was performed in eTomo, which is part of the IMOD software package, and additional cropping was done if necessary.

2.8 Thick Section Tomography Image Acquisition

For thick section tomography, 3 µm serial sections were cut. They were carbon coated on both sides, and 30 nm gold particles were placed on both the top and bottom. Each section was placed on a separate 75mesh folding grids. These grids were imaged at 3 MeV on the UHVEM with a 4k x 4k CCD camera. The magnification was 5000x. These 3 µm serial section samples were processed and found to have very little contrast, so the samples were later post stained with a second round of UA and lead to increase contrast. Additionally, 60 nm gold particles were applied.

2.9 SBFSEM Image Acquisition

Following the embedding procedure for the slice prepared for SBFSEM, the photoconverted cell was cut out and mounted on an aluminum pin using cyanoacrylate glue. The sample was trimmed, and the sides were grounded to the

pin using silver paint. The complete block was then coated with a thin layer of gold-palladium.

A 3 x 3 mosaic with 10% overlap was collected on the 3View system using a backscatter detector. Each tile was taken at 3000x magnification and 6144 x 6144 resolution, with a pixel size of 5.6 nm and a step size of 70 nm. The chamber pressure was 30 Pa, the beam current was 2.5 keV, and the spot size was set to 2.5.

2.10 LM Deconvolution

Following collection of the LM image stacks, deconvolution was performed to reduce the out-of-focus haze and blur caused by the bending of light as it hits the specimen. Deconvolution can improve the signal to noise ratio as well as the spatial resolution. The raw data files were transferred to AutoQuant X (AutoQuant Imaging; Waterviet, NY), a deconvolution tool. The program was set to 10 iterations of deconvolution using the adaptive blind deconvolution algorithm, and the resulting image is shown in Figure 2.3**.**

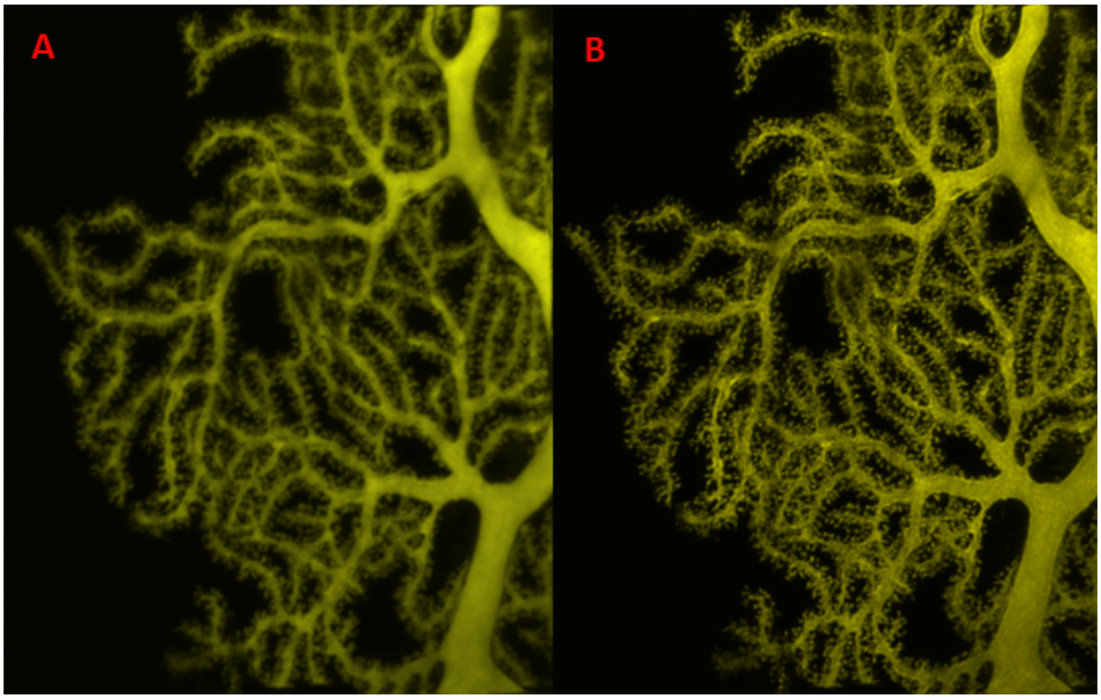

Figure 2.3 Raw (A) and deconvolved (B) light microscopic volumes of a portion of LY-filled Purkinje cell dendritic trees illustrating the increased clarity of the dendritic shaft and spines in the deconvolved image.

2.11 Surface Rendering and Segmentation

2.11.1 LM Data

After deconvolution was performed on LM image stacks, each dendritic segment and its spines were segmented. Due to the difficulty of tracing spines at the LM level, three different methods were evaluated to find the optimal one for this investigation. First, the Filament Tracer in the commercially available program, Imaris (Bitplane, Zurich, Switzerland), was used, which segments spines from the 3D volume. Both the semi-automatic and manual modes were used for comparison.

Next, Neurolucida (version 9.0) was used for manual segmentation. To segment the dendritric shaft, a line was placed along the center of the shaft on the slice showing the dendrite most fully in view while flipping through the image stack.

To draw the line, the scroll wheel on the mouse was adjusted to match the diameter of the dendritic shaft. Points were placed along its length, making sure that the scroll wheel was continually adjusted.

Once the dendritic shaft was traced, a specific set of steps were used to segment the spines, in an effort to segment spines consistently on each dataset. After tracing the dendritic shaft, a line was drawn to represent each spine closest to the shaft in the XY plane. When a spine was located, it was traced on the slice where the spine head appeared furthest away from the shaft. The spine head also tended to be brightest on this slice. The contrast was adjusted several times while flipping through the image stack to ensure all spines in the XY plane were traced. Once all spines in the XY plane were covered, spines in the Z plane were traced by placing a line from the brightest spot, representing the spine head, back to the shaft. Again, the contrast was adjusted several times while flipping though the z stack. Since spines in the Z plane were often partially hidden by the dendritic shaft, it was especially crucial to adjust the contrast and flip back and forth in Z to ensure no spines were missed. To reduce bias in counting the spines, each dataset was manually segmented three separate times, and the spine density, dendritic length, and dendritic diameter values were averaged.

Following manual segmentation of the image stacks in Neurolucida, quantitative analysis of the dendrites and spines was done in Neurolucida Explorer. An algorithm in the program was used to provide dendritic spine density, distance from the soma, and diameter of the dendritic segment.

2.11.2 EM Data

After serial section tomograms were stacked to create the full volume, they were ready for spine density analysis.

Data collected from each of the three electron microscopes were analyzed in IMOD. 9 dendritic segments from serial section tomography, one dendritic segment from thick section tomography, and 8 dendritic segments from SBFSEM were analyzed. To determine the length of a dendritic segment, a line was drawn through the center of the dendritic shaft, which was parallel to the Z plane. Spines were then marked by placing points at the spine head. The resulting model is illustrated in Figure 2.4. Similar to the LM data, the EM spine counts were done by repeatedly flipping through the Z slices to ensure all spines were marked. In order for a spine to be marked, its neck had to be followed back to the dendritic shaft, to confirm that it belonged to the dendritic segment of interest and not a neighboring dendrite. Spine density was determined by counting the total number of spines and dividing by the length of the dendritic segment and is presented in the remaining sections as number of spines per unit length.

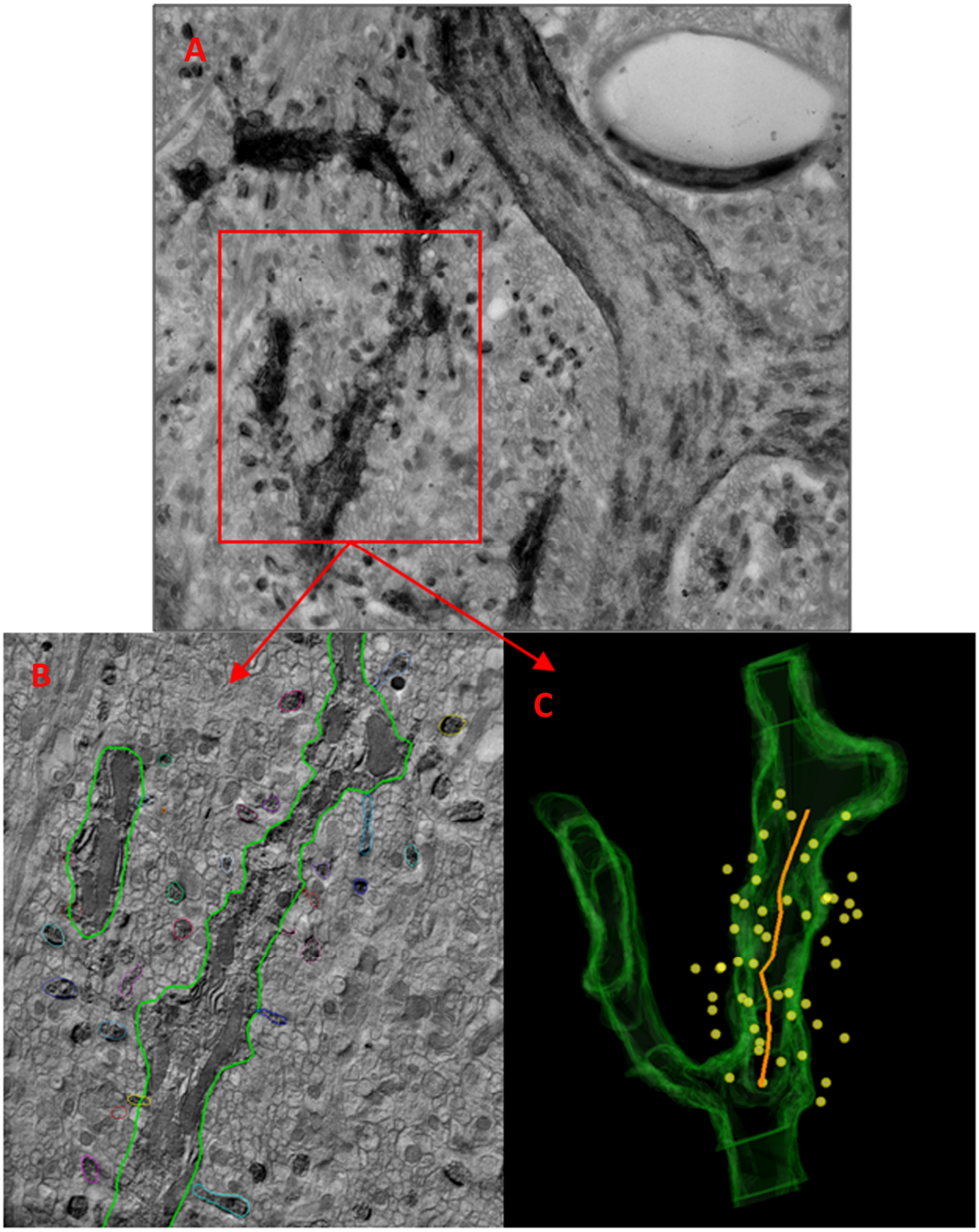

Figure 2.4 EM image and segmentation of a dendritic segment from serial section tomography chosen for analysis. The raw image before reconstruction is shown in A. The dendritic shaft and spines were fully traced in only a few datasets as shown in B. In all datasets, spine density was found by drawing an orange line along the length of the shaft and placing yellow spheres to mark locations of spines as shown in C.

The diameter of each dendritic segment was found by drawing a line each at the beginning, middle, and end of the length of the segment, and averaging the three values.

At least one dataset from each electron microscope was fully segmented and rendered for visual purposes. Manual segmentation was performed in IMOD (version 3.13.5).

Movies of the segmented volumes were made using Amira (Mercury/TGS, San Diego, CA) for 3D visualization.

An adaptation of the text and figures from Chapters 1, 2, 3, and 4 will be submitted for publication with the following co-authors: Eric Bushong, Maryann Martone, Mark Ellisman, Naoko Yamada, Andrea Thor, Erik De Schutter, and Masako Terada. The thesis author was the primary contributor to the work of this chapter.

CHAPTER 3: RESULTS

3.1 Dendritic Spine Density

3.1.1 Comparison of LM Segmentation Tools

Three separate segmentation tools were evaluated before selecting the optimal one for analysis of LM volumes: 1) semi-automatic segmentation in Imaris, 2) manual segmentation in Imaris, and 3) manual segmentation in Neurolucida. When segmenting the identical dendritic segment using each tool, three different spine density values were found as shown in the example in Figure 3.1. Spine density was 2.55 spines/µm when semi-automatically segmented in Imaris, 4.67 spines/µm when manually segmented in Imaris, and 5.69 spines/µm when manually segmented in Neurolucida. In this example there was a 55% difference between the semi-automatic segmentation in Imaris and the manual segmentation in Neurolucida. When rotating the volume in 3D in Imaris, it was obvious that many spines had been missed with the semi-automatic segmentation, and some spines of neighboring dendrites had been mistakenly traced. When using manual segmentation in Imaris, it was very difficult to see spines in the z plane, because these spines were blurred when rotating the volume in 3D. After careful evaluation of each tool, we decided to use Neurolucida to manually segment the remaining dendritic segments.

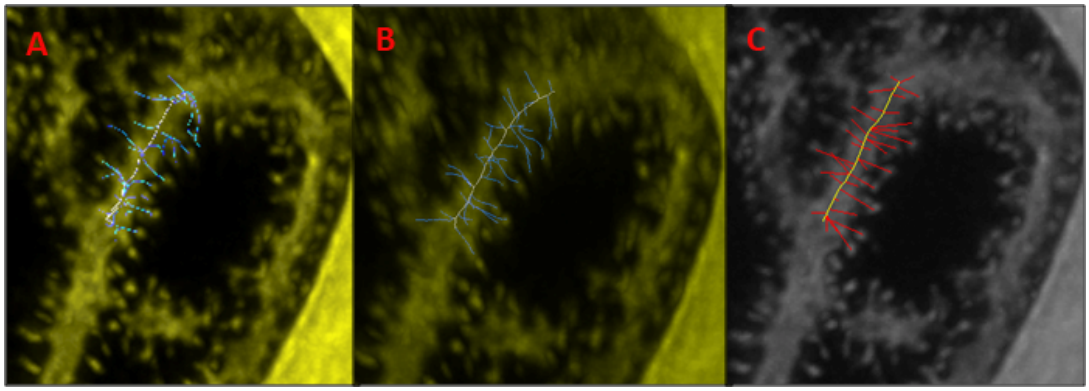

Figure 3.1: Comparison of spine segmentations across three segmentation tools that were evaluated for this investigation. For the same dendritic segment, spine density was 2.55 spines/µm when semi-automatically segmented in Imaris (A), 4.67 spines/µm when manually segmented in Imaris (B), and 5.69 spines/µm when manually segmented in Neurolucida.

3.1.2 LM vs. EM Spine Density

LY dye successfully filled the dendrites and spines of Purkinje cells as shown in Figure 3.2. Confocal microscopic volumes of LY-filled Purkinje cells revealed an average spine density of 5.97 $\pm$ 0.96 spines/µm (Figure 3.3). Spine density values varied minimally across each animal and cell. When tracing the spines manually in Neurolucida, it was difficult to resolve each spine and sometimes a small amount of guesswork was necessary. Thus, to minimize error, each dendritic segment was traced three times in Neurolucida, with average values presented in Figure 3.4.

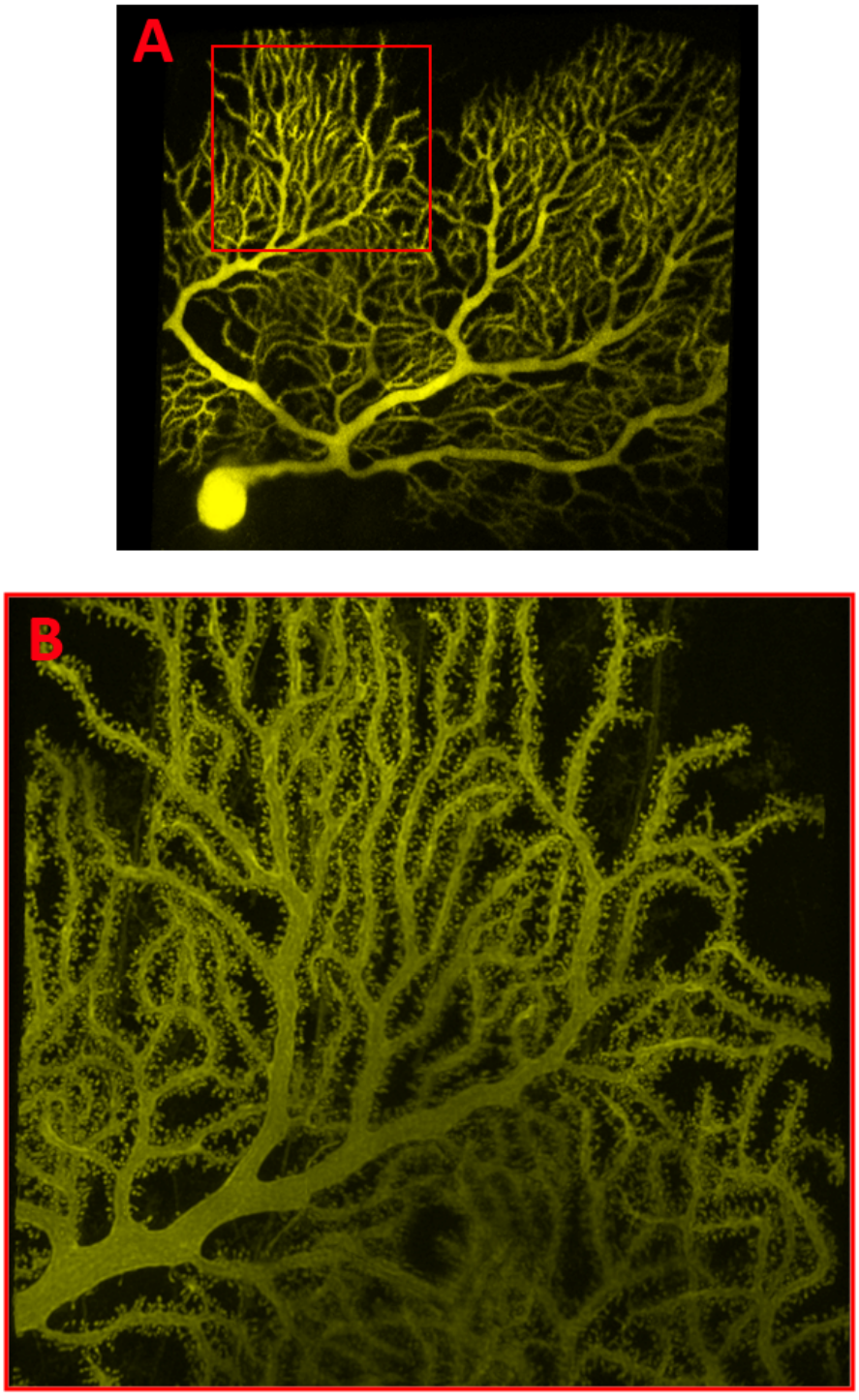

Figure 3.2: Single slices from light microscopic volumes of a Purkinje cell collected on the FluoView showing successful LY injection. (A) Whole cell collected on the FluoView at 20x magnification. (B) A portion of the whole cell (boxed region in A) was collected on the FluoView at 60x magnification for the correlated study.

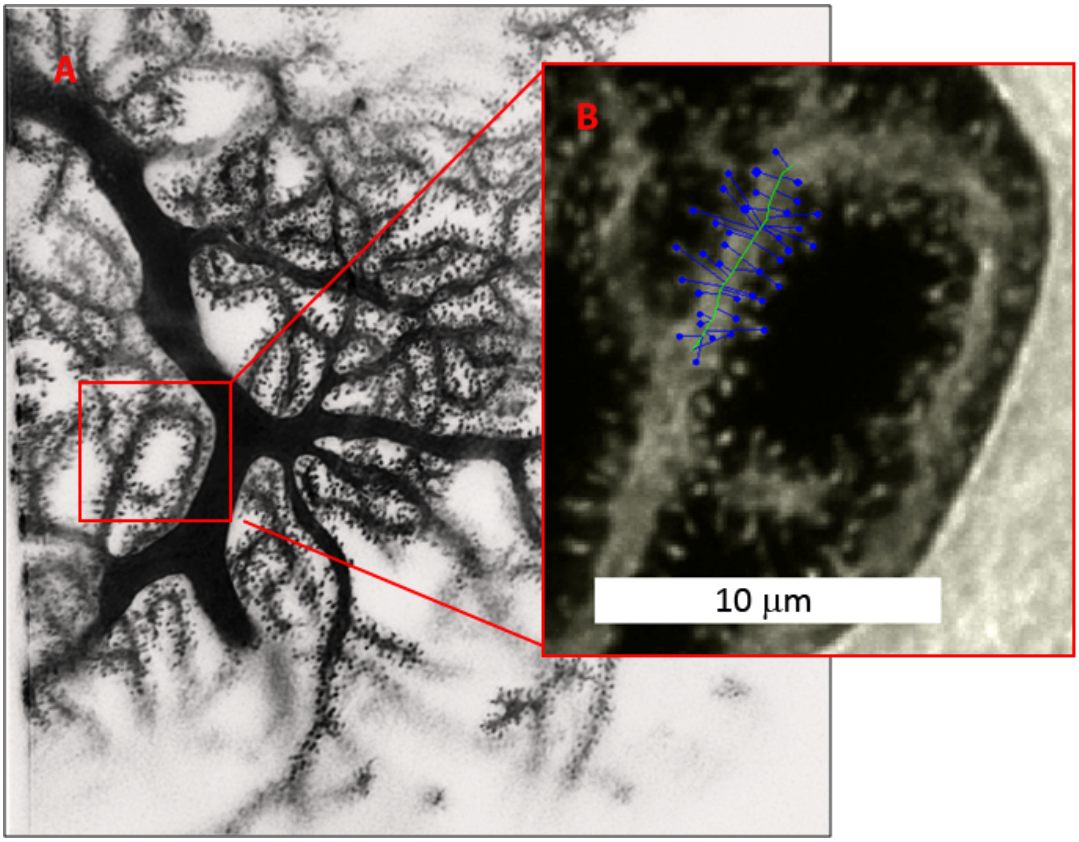

Figure 3.3: Representative confocal microscopic volume of a region from a LY-filled Purkinje cell. (A) Maximum intensity projection. (B) The dendritic segment chosen for spine density analysis was manually traced in Neurolucida.

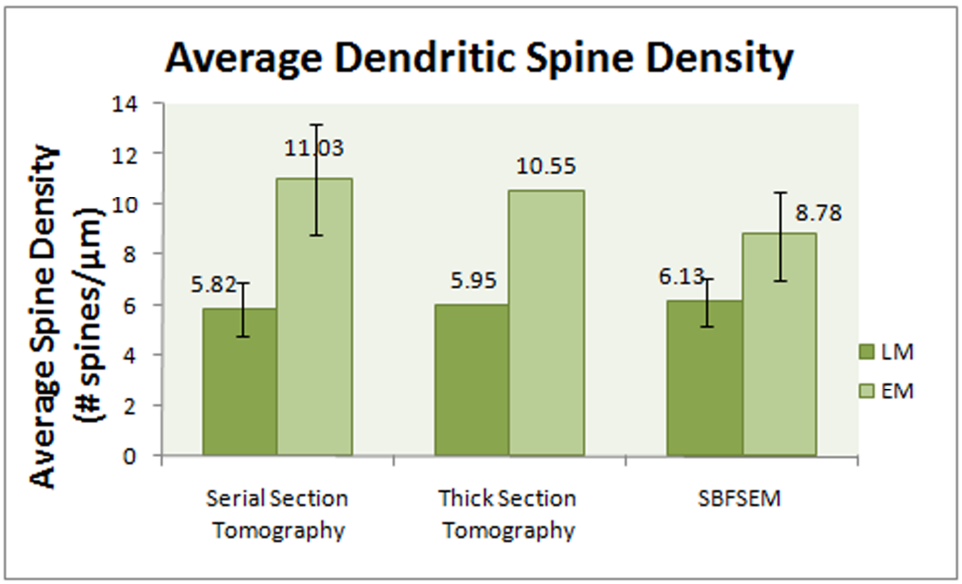

Figure 3.4: Comparison of average spine density from dendritic segments collected from both LM and EM. The three separate EM techniques used are shown. Error bars represent the standard deviation.

As expected, LM volumes revealed lower spine counts than the corresponding EM volumes by an average of 40 ± 11.18%. The highest spine density was found using serial section tomography at 11.03 ± 2.20 spines/μm, followed by thick section tomography with 10.53 spines/μm and SBFSEM with 8.78 ± 1.78 spines/μm (Figures 3.5 and 3.6). LM spine density values are 46.36 ± 8.42% lower in serial section tomography compared to 43.62% lower in thick section tomography and 30.23 ± 6.70% lower in SBFSEM. The percent differences are illustrated in Figure 3.6 below.

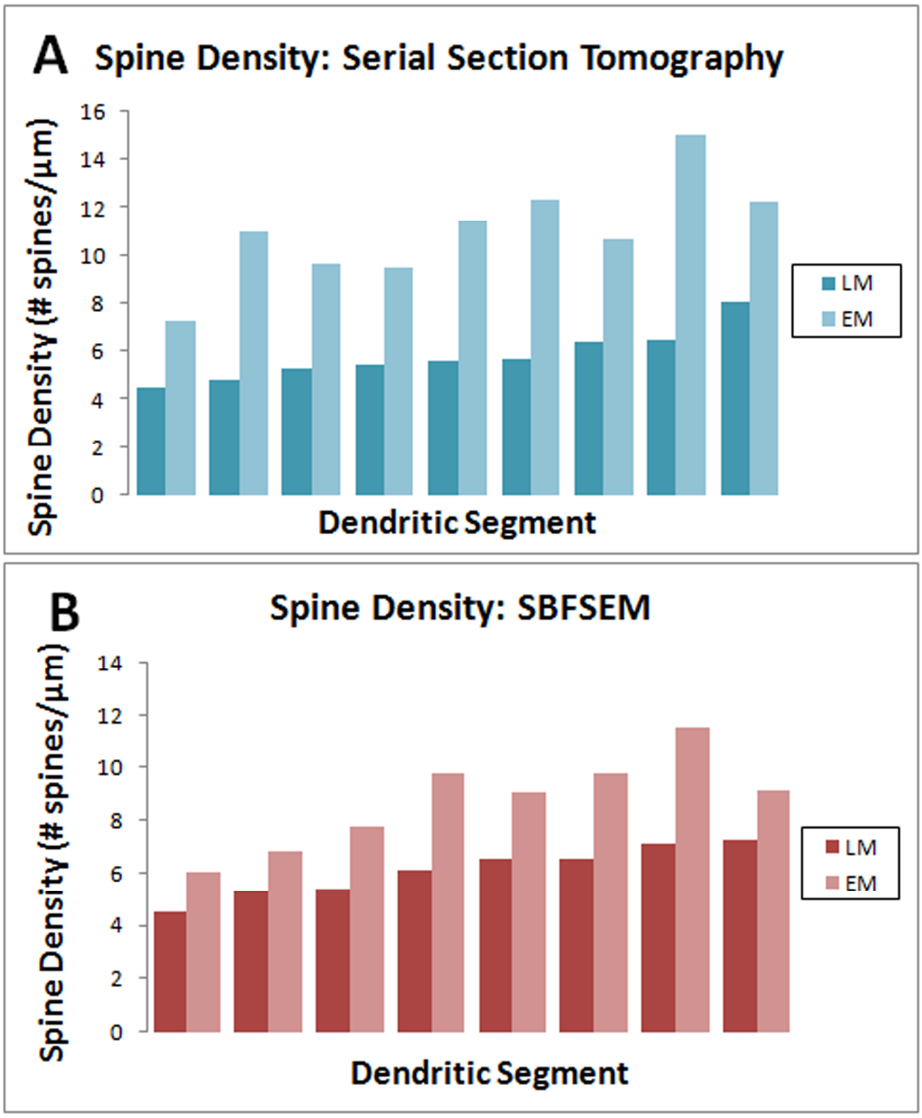

Figure 3.5: Comparison of spine density on each dendritic segment collected from both LM and EM using serial section tomography, thick section tomography (A), and SBFSEM (B).

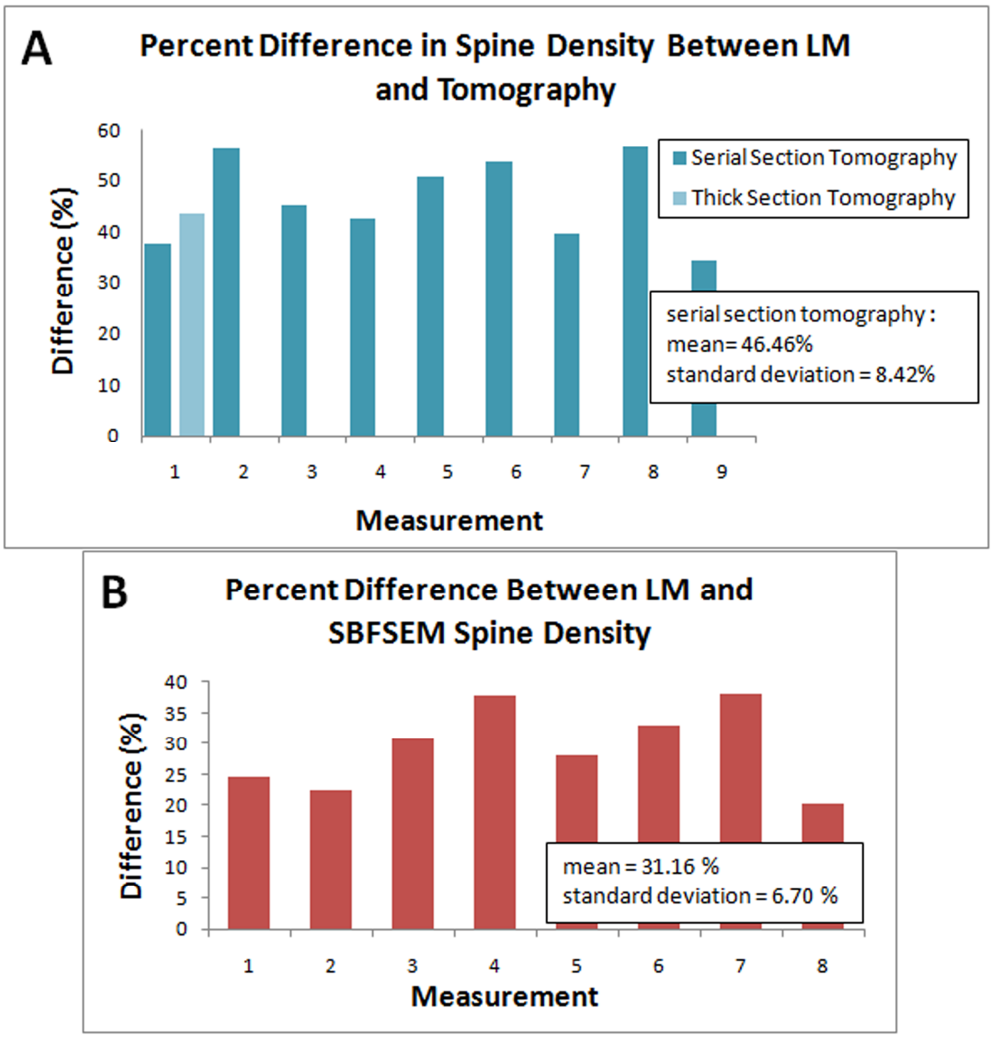

Figure 3.6: Percent differences in spine density from LM to EM for each dendritic segment using serial section tomography, thick section tomography (A), and SBFSEM (B).

3.2 Dendritic Diameter

When selecting dendritic segments, we ensured that a range of diameters was used, from 0.62 μm to 2.62 μm. At the LM level there is a slight increase in dendritic spine density as diameter increases (R^2 value: 0.559). There is no evidence for a relation between dendritic diameter and spine density for serial section tomography (R^2 value: 0.065), but the results indicate an increase in dendritic spine density as

diameter increases for SBFSEM (R^2 value: 0.561). Scatter plots of the results are shown below in Figure 3.7.

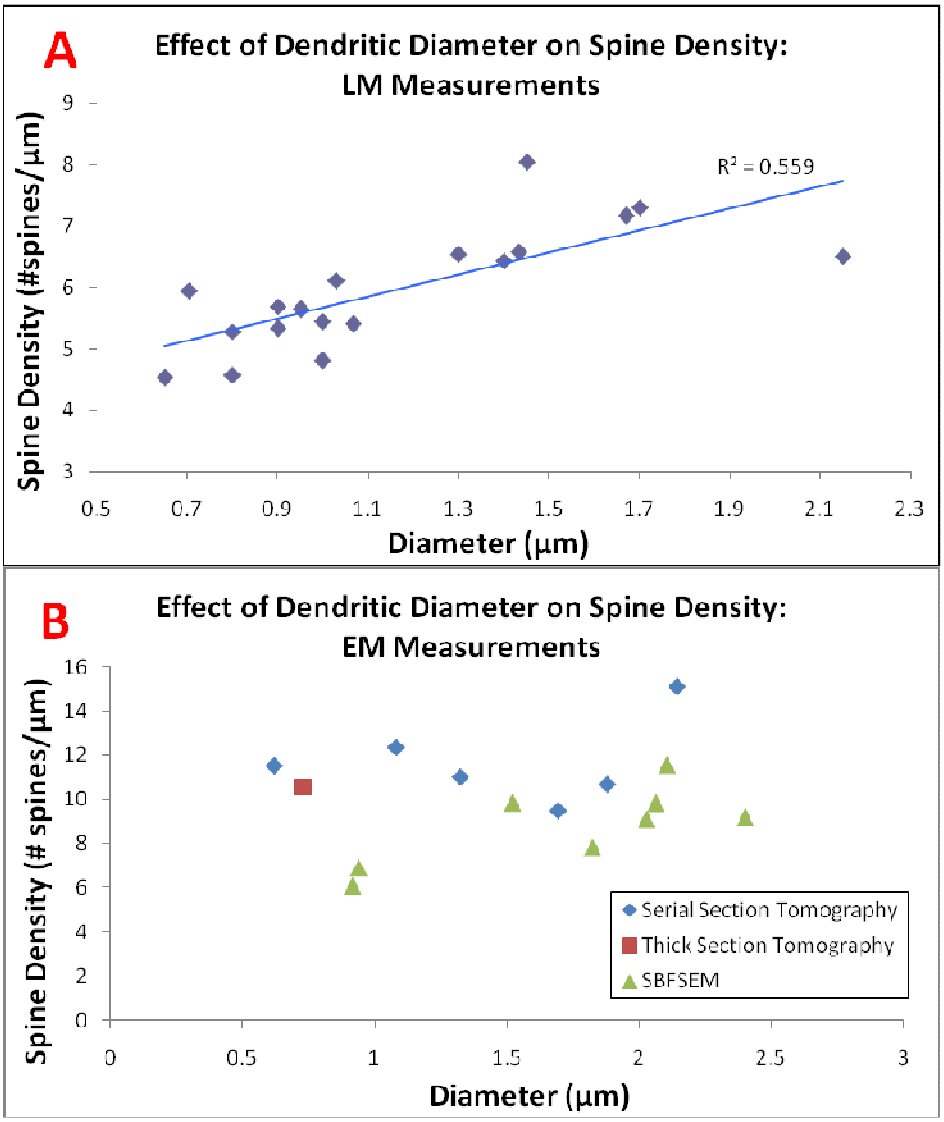

Figure 3.7: Relationship between dendritic diameter and spine density for both LM (A) and EM data (B).

3.3. Dendritic Distance From Soma and Branch Order

In order to determine each dendritic segment's distance from the soma and branch order, 20x low magnification images of the fluorescent cells and 60x mosaics of the photoconverted cells were collected on a FluoView confocal microscope. As

shown in Figure 3.8 the shape of the dendritic tree varied by cell, but each was very dense with dendrites and spines.

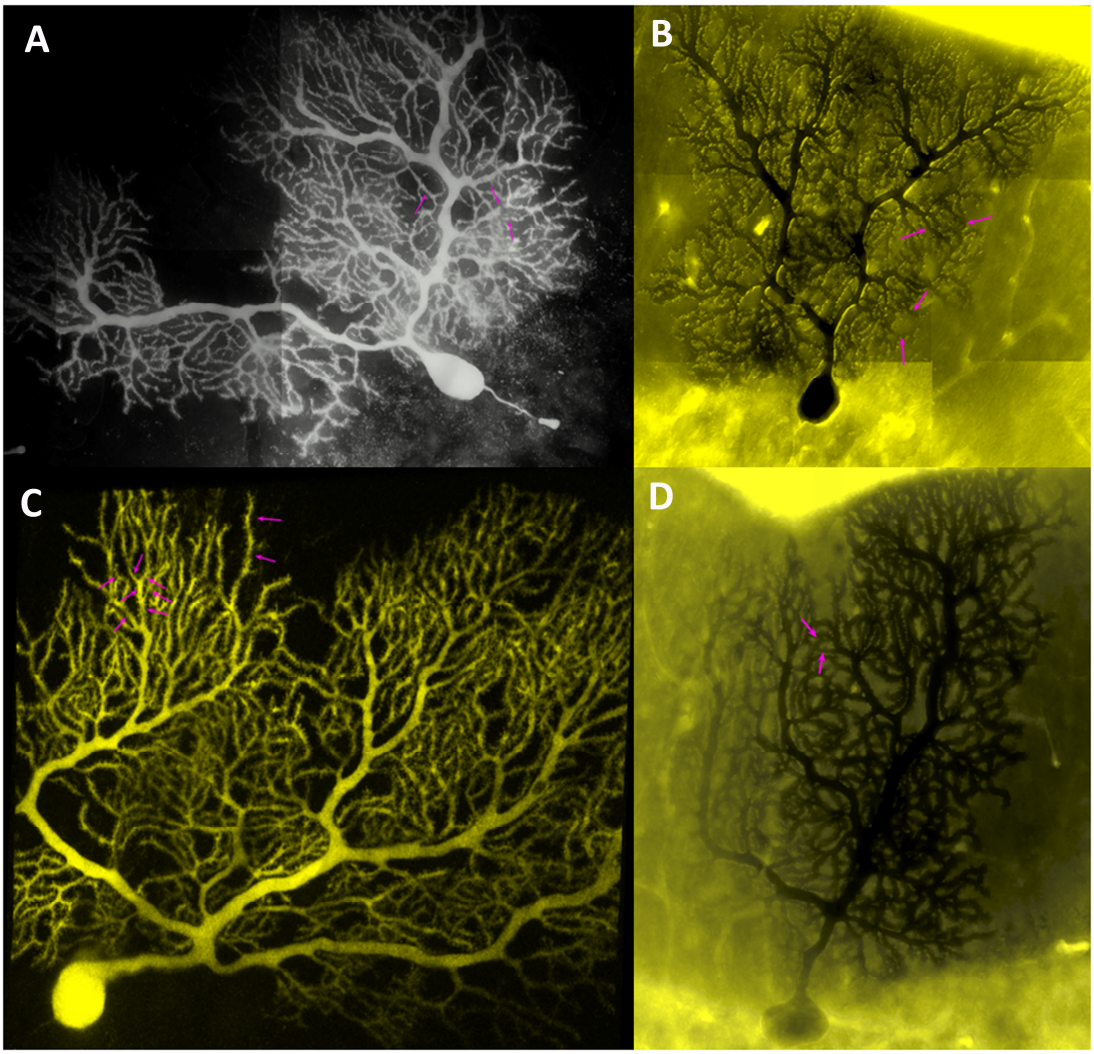

Figure 3.8: Confocal microscopic volumes of the whole Purkinje cells showing the variation in the shape of each dendritic tree. Arrows point to the particular dendritic segments chosen for correlated spine density analysis. Cells in A and B are from Animal 2, and cells from C and D are from Animal 3. Cells in A and B are mosaics collected at 60x magnification on an Olympus FluoView, the cell in C is an image stack collected at 20x magnification on the Olympus FluoView, and the cell in D is an image stack collected at 20x magnification on an Olympus DSU.

We selected dendritic segments located at a specific distance from the Purkinje cell soma that fell into a particular range. The closest dendritic segment was

81.6 µm from the soma, while the furthest was 280.5 µm from the soma. In LM volumes, there does not appear to be a correlation between distance from soma and spine density (R^2 value: 0.047) or between branch order and spine density (R^2 value: 0.011). EM data suggests a relationship exists between dendrite distance from the soma and branching order as seen in Figure 3.9 and Figure 3.10. The data suggests that spine density may decrease as the distance from the soma and branch order increases. However, there is no relationship between dendrite distance from soma and spine density *within* each imaging technique (R^2 values are 0.059 for serial section tomography and 0.043 for SBFSEM). There is also no relationship between branch order and spine density *within* each imaging technique (R^2 values are 0.043 for serial section tomography and 0.033 for SBFSEM)

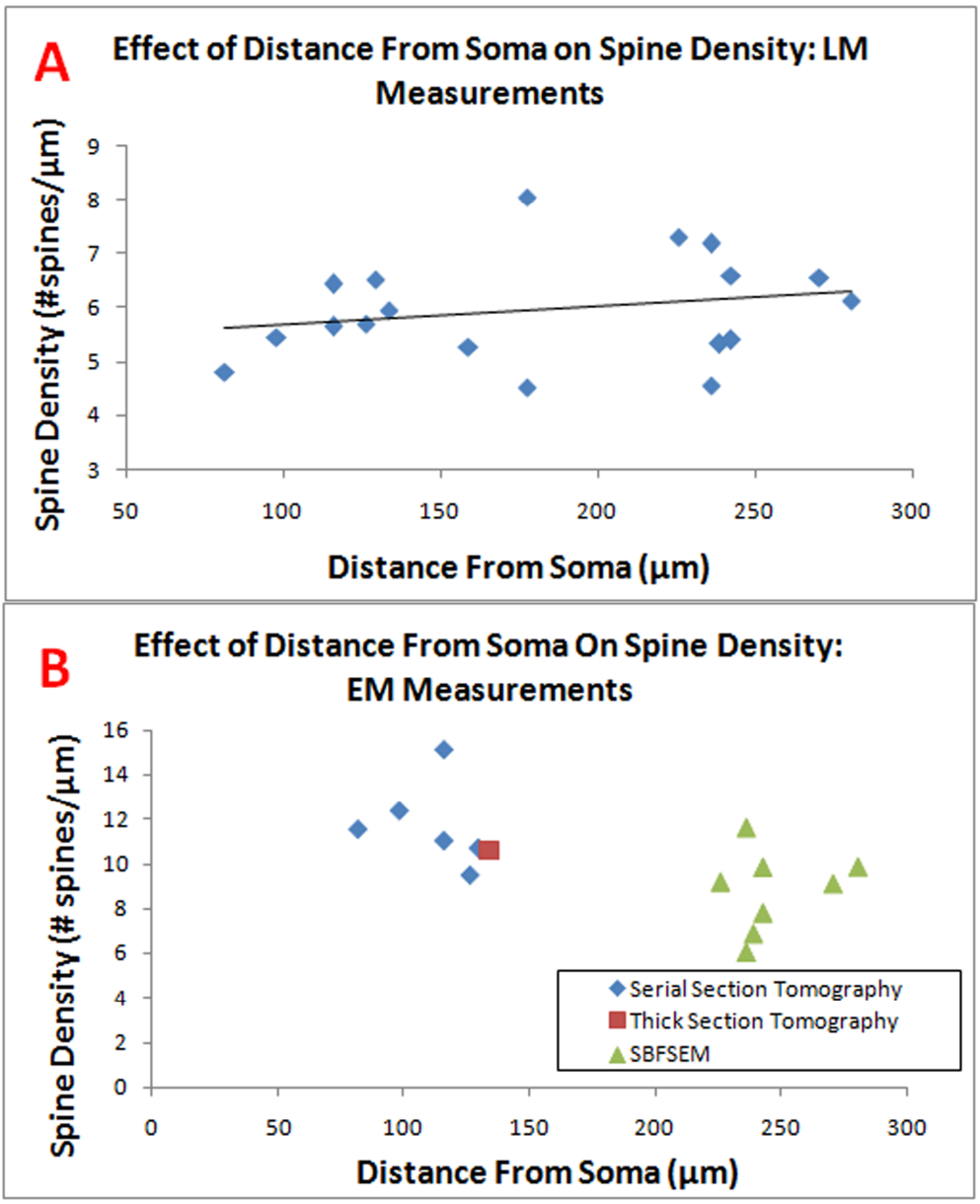

Figure 3.9: Relationship between dendritic distance from the soma and spine density for both LM (A) and EM (B).

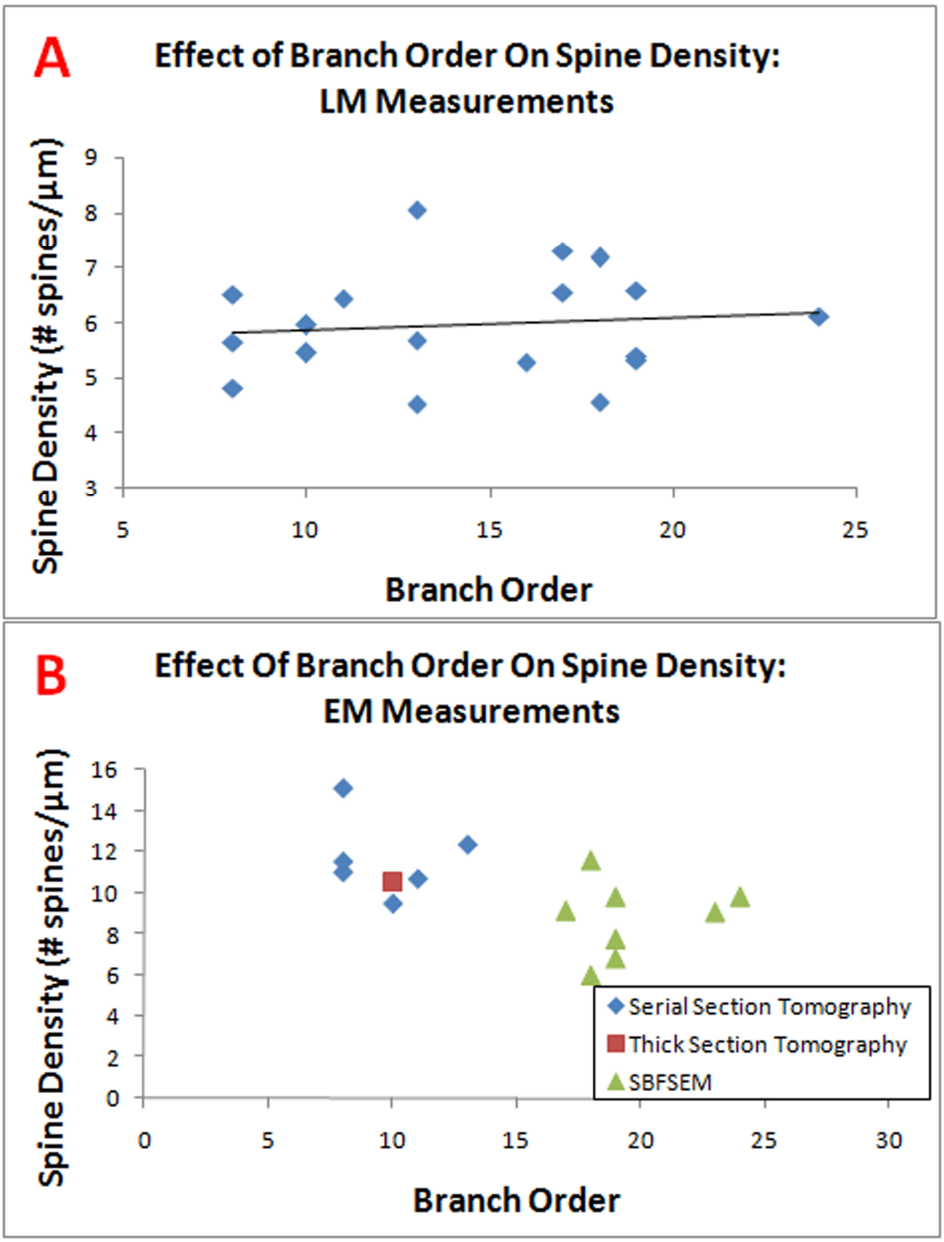

Figure 3.10: Relationship between branch order and spine density for both LM (A) and EM (B).

An adaptation of the text and figures from Chapters 1, 2, 3, and 4 will be submitted for publication with the following co-authors: Eric Bushong, Maryann Martone, Mark Ellisman, Naoko Yamada, Andrea Thor, Erik De Schutter, and Masako Terada. The thesis author was the primary contributor to the work of this chapter.

CHAPTER 4: DISCUSSION

The primary findings of this investigation are that dendritic spines of Purkinje cells occur at a density that is 40% lower using LM imaging and analysis compared to an EM approach. A higher spine density was expected in EM, since resolution limitations in the light microscope sometimes cause spines to be obscured by dendritic shafts or neighboring spines. This is especially true in the Purkinje cell where dendrites and spines are so dense. Limits in resolution also cause difficulty in resolving spine necks, making it challenging to follow a spine back to its parent dendrite. The results of this study on spine quantification are discussed in detail below.

4.1 LM vs. EM Segmentation

It is surprising that the spine density difference is so large between LM and EM findings. Despite a number of segmentation tools available, it remains challenging to trace spines in LM. Three tools were carefully evaluated to determine the optimal one for this investigation. In all cases, resolution limits in the light microscope remain a key challenge. It is difficult to resolve spine necks, and neighboring spines may overlap, making it difficult to distinguish two separate spines as well as branched spines. Branched spines could be misinterpreted as two separate spines if only the spine heads and not the necks were visible. In EM it was easier to identify branched spines, but in a few cases the branch point was very close to the dendritic shaft. Thus, it was difficult to determine if this was a branched spine or two separate spines. Still, since this occurred in just a few cases, the overall effect on spine density results would be minimal.

Additionally, it is possible that all spines were not filled with LY or during photoconversion and could go undetected in LM and EM images, but this was carefully analyzed in both the LM and EM images and no unfilled spines were discovered. The first segmentation tool used was the semi-automatic segmentation mode of the Filament Tracer in Imaris, which segments the spines from the 3D volume. In order to trace the spines and ensure that no spines were missed, the volume must be rotated in 3D. The semi-automatic segmentation method missed several spines and sometimes segmented spines as dendrites. In the end, it required more time to correct these mistakes than to manually trace the spines. The manual mode in the Filament Tracer was also used, but it was still challenging to resolve spines in 3D, and spines were often obscured by the dendritic shaft or by neighboring spines or dendrites when rotating the volume (Figure 4.1).

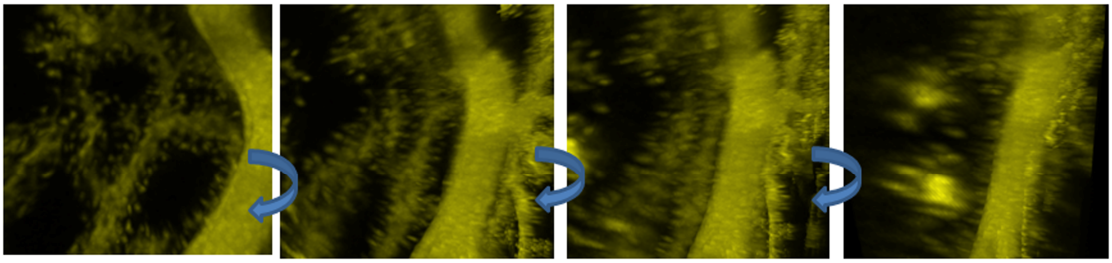

Figure 4.1: Representative images from a confocal microscopic volume as it is rotated. The visibility of spines decreases as the volume is rotated, and in some cases the spines are obscured by the shaft, as seen in the far right. Spines projecting off the sides of the dendrite (left) are more visible than those projecting in z, off the front and back (right).

After experimenting with Imaris, it was determined that manual segmentation in Neurolucida was the optimal choice for analyzing spine density in LM. Neurolucida allows the user to trace spines by flipping through the z stack instead of working with the full 3D volume, making it easier to follow a spine back to its parent dendrite. To further minimize error, each dendritic segment was traced three times in Neurolucida,

and spine density, length, and diameter values were averaged. Although manual segmentation of LM volumes in Neurolucida worked reasonably well, EM data was superior in resolution and spines could be resolved much more easily. It appears that spines missed in LM volumes are those projecting from the front and back of the dendrite, as seen in Figure 4.1. In EM volumes, spine necks could easily be followed back to the dendritic shaft in images from serial section tomography and SBFSEM. Photoconverted spines appeared dark and dense, and they were easily distinguished from neighboring structures such as vesicles and mitochondria.

4.2 LM vs. EM Spine Density

Results presented in Section 3.1.2 indicated that spine density was 40.07 ± 11.18% lower in LM compared to EM. Since it was evident that spines were missed in LM volumes, LM spine density values were normalized to EM values, using the mean percent difference (Figure 4.2). Nearly all of the normalized LM values fall within one standard deviation of the corresponding EM values. The standard deviation is fairly large, and this may be due to a low number of samples. Although we are limited in our sample size, the data in these graphs further indicate a 40% difference in spine density from LM to EM and this normalization factor can accurately be applied to LM values.

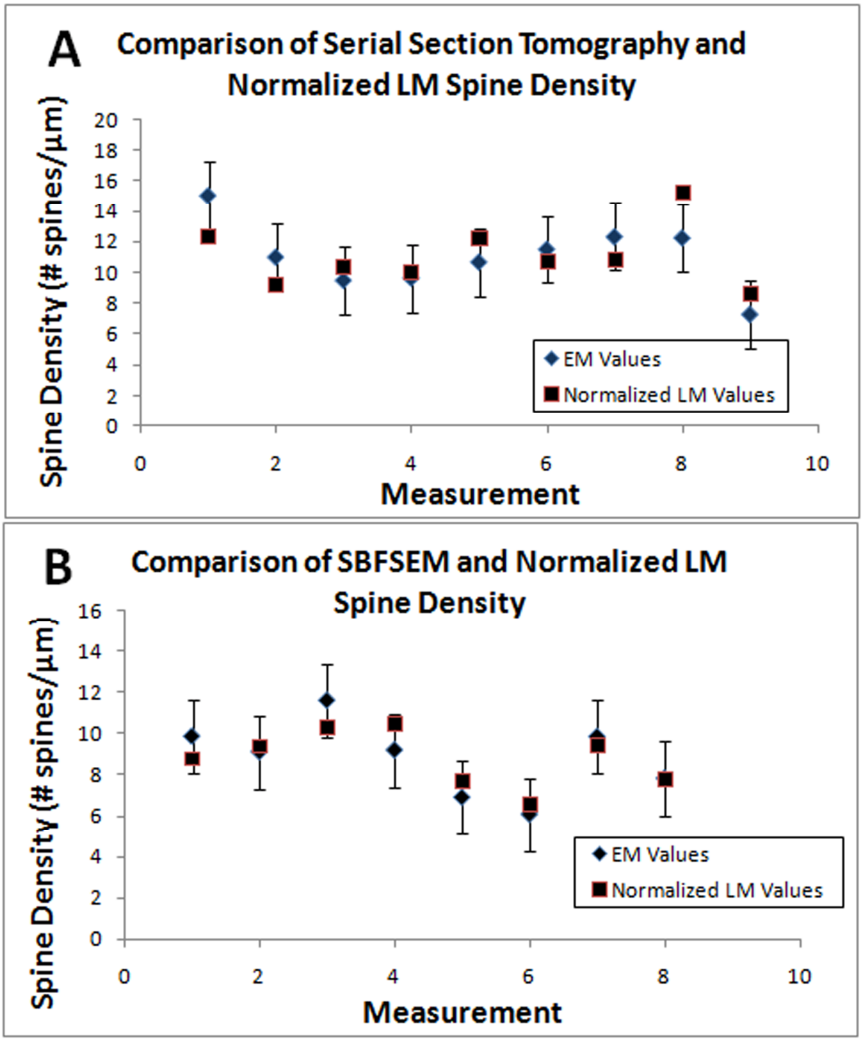

Figure 4.2. LM spine density values normalized to the EM techniques, serial section tomography (A) and SBFSEM (B), based on the mean percent difference. Error bars represent the standard deviations of the EM values, and nearly all of the normalized LM values fall within one standard deviation of the corresponding EM value.

4.3 Thick Section Tomography

While serial section tomography and SBFSEM produced high quality images for this investigation, few conclusions can be drawn from data collected using thick section tomography. Images collected on the UHVEM for thick section tomography resulted in poor contrast, making it difficult to resolve spines. Thus, only one dendritic segment was analyzed. Still, the spine density value for this EM dataset (10.53

spines/μm) is comparable to values found for serial section tomography and SBFSEM, so we included it in the analysis.

4.4 SBFSEM

There was a smaller difference in spine density between LM and EM (30%) when using SBFSEM. The average spine density was also lower compared to that of serial section tomography (8.78 spines/μm vs. 11.03 spines/ μm, respectively). It is important to note that the average length of a dendritic segment used for SBFSEM was longer (11.51 μm compared to 7.84 μm). Although spines could be followed fairly easily, the resolution still falls behind that of serial section tomography. The larger z-step size (70 nm) causes a greater loss of tissue in between slices. SBFSEM is also challenging in that the block face is completely black, due to very heavy metal staining required. This makes it extremely challenging to determine the area of the cell from which the correlated LM images were collected. Since it is nearly impossible to see anything, guess work is necessary. It may take a long time until the area is found. Once the area is located, SBFSEM is advantageous because the image collection is automated, and image processing time is much quicker than any other EM method. However, since spine density values are lower in SBFSEM compared to serial section tomography, more research is needed to determine the reasons for the discrepancy.

4.5 Specimen Shrinkage

Even though serial section tomography and SBSEM produced images that improved spine density quantification, these methods are certainly not free from potential errors. Specimen shrinkage and distortions may occur as a result of the

fixation procedure, dehydration procedure, embedding procedure, and prolonged irradiation from the electron beam. When electron irradiation occurs at conventional illumination levels, it may cause specimen shrinkage normal to the plane of the sample (Willis, 1973; Bennett, 1974). The degree of shrinkage could depend on many factors including type of fixatives, type of resin, accelerating voltage, magnification, and duration of exposure to the electron beam. We used a low dosage of glutaraldehyde (4% PFA and 2% glutaraldehyde) for a low duration of time in an attempt to minimize shrinkage during the fixation procedure. We attempted to allow all shrinkage induced by the electron beam to take place before collecting the tilt series by "cooking" the sample as discussed in the Methods section. Previous studies have reported minimal shrinkage in the lateral plane but shrinkage in the depth dimension by as much as 50% (Bennett, 1974).

One previous study was performed in our lab by Tom Deerinck on skeletal muscle. Although the work is unpublished, tissue shrinkage was evaluated carefully utilizing parameters similar to those in the present study. The tissue was embedded in Durcupan and sectioned for an IVEM. The sample was placed in the microscope at a high magnification and was irradiated at the largest spot size of 1 for 2-3 hours. Since a high magnification was used from the start, the sample was not surveyed at low magnification, and tissue shrinkage at low magnification was not a factor. A tilt series was not collected due to difficulty in locating the area, but the duration of irradiation is similar to the time that would be spent collecting a tilt series.

Following irradiation, the sample was taken out, and a black spot was visible at the location of irradiation when viewed under a light microscope. The sample was then turned on its side, reembedded, and sectioned again at 0.5 µm. Measurement of the irradiated thickness compared to the unirradiated thickness is shown in Figure

4.3. This ratio represents the shrinkage in z due to the electron beam, and it was found to be 12.5%.

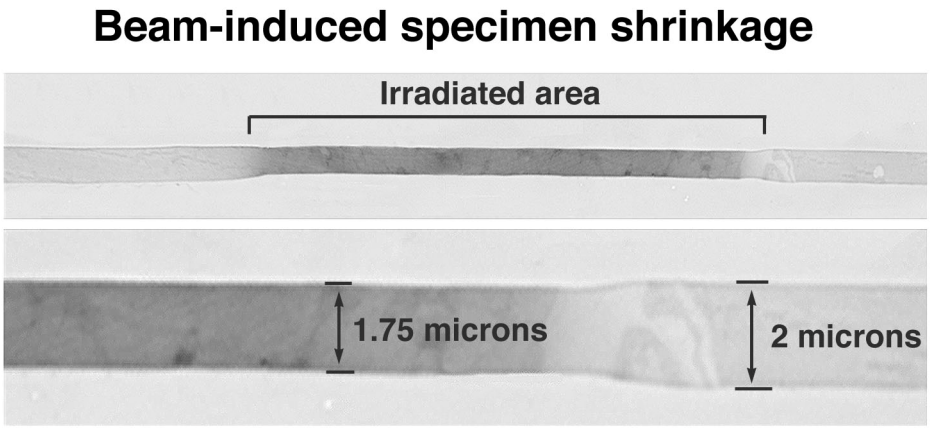

Figure 4.3: Specimen shrinkage resulting from the electron beam. Printed with permission by Tom Deerinck.

If the dendrites were perfectly oriented in the z direction, a 12.5% shrinkage would maximally increase the spine density by 14.29%. In this investigation, all of the dendrites were oriented roughly parallel to the section plane, orthogonal to z. Thus, the increase in spine density due to shrinkage in z must be much less than 14.29%. Therefore, shrinkage in z contributes very little to the measured difference in spine density between LM and EM.

4.6 Dendritic Diameter

There may be a relationship between dendritic diameter and spine density, but this was more evident in SBFSEM volumes than serial section tomography volumes. The methods utilized to acquire diameter measurements are not free from error. In LM volumes, limits in resolution make it difficult to collect diameter measurements. There is also user variability in that one may adjust the mouse scroll wheel slightly more than another user. This could lead to a large difference in the overall diameter

of the dendritic segment. Due to this potential for error, the diameter of each dendritic segment was measured three times in Neurolucida in this investigation, and the average was used.

Additionally, it was challenging to accurately measure the diameter of dendritic segments from EM volumes. We are aware that our method of measuring the diameter at the beginning, middle, and end of the length of the dendritic segment is only a rough estimate of the diameter. Although the dendritic shaft is often thought of as being cylindrical in shape, it constantly changes in diameter throughout its length as seen in EM volumes (Figure 4.4).

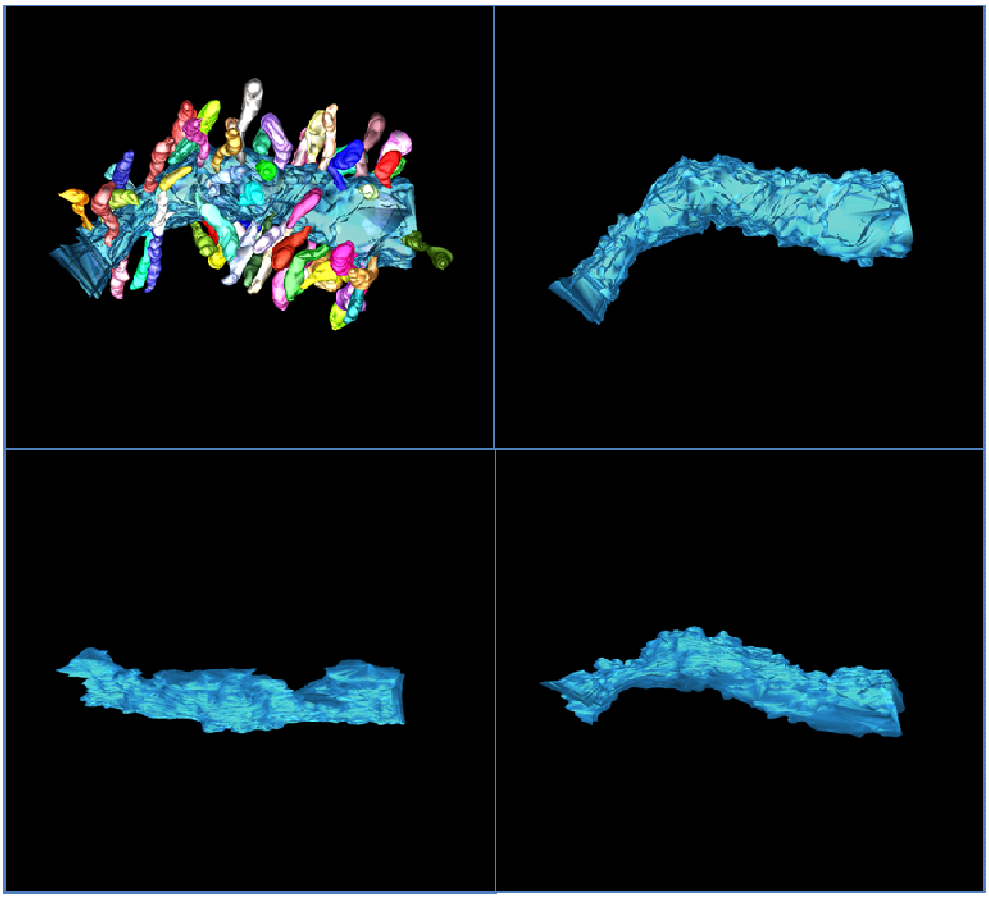

Figure 4.4: Representative surface rendering of a dendritic segment collected using serial section tomography. The full segment is shown with its spines (upper left), and the dendritic segment is rotated at different angles to show the variation of dendritic diameter along the length of the segment.

As seen in Figure 3.7, the range of diameters for both serial section tomography and SBFSEM is similar, from about 0.75 µm to 2.25 µm. Thus, it is likely that additional dendritic segments need to be analyzed to determine whether spine density varies with dendritic distance from the soma and branch order.

4.7 Dendritic Distance From Soma and Branch Order

It appears that both distance from soma and branch order may be correlated with spine density at the EM level as seen in Figures 3.9 and 3.10. However, this may be caused largely by clustering of the data based on the particular EM technique as opposed to a biological difference. The overall area chosen for serial electron tomography was closer to the soma and had a lower branch order than the overall area chosen for SBFSEM. These areas were chosen by visual inspection before the distance from the soma was measured.

One way to better evaluate this potential relation is to measure the dendritic distance from the soma and branch order immediately after collecting low magnification fluorescent volumes of the entire cell and before acquiring high magnification fluorescent volumes. Since time is already a factor in a correlated study, this step must be accomplished carefully yet quickly in order to minimize degradation to the tissue samples.

4.8 Conclusions

It is a challenge to count dendritic spines in the Purkinje cell, and previous studies have generated a wide range of spine density values. There are many factors that must be considered, including imaging modality and sample preparation protocol, and the goal of this investigation was to minimize these variables by

employing correlated LM and EM. The higher spine density values found in the electron microscope are largely due to improvements in axial resolution compared to the light microscope, making it significantly easier to resolve spines. Axial resolution in serial section tomography is around 10 nm and in SBFSEM is 140 nm. Purkinje cells are especially dense with spines, and the values we found in the electron microscopic volumes are comparable to some of the higher densities (e.g. 11-14 spines/µm) originally reported by Harris and Stevens.

This research presents the first correlated study utilizing both LM and EM on Purkinje cell dendritic spines. Since our results indicated that both the dendritic distance from the soma and branch order may have a relationship to spine density, future work should focus on whether this is due to a difference in imaging technique or a biological difference.

Additionally, spine density values found in this investigation could indicate a link to the circuitry of the cerebellar cortex. Climbing fibers synapse on more proximal portions of Purkinje cell dendritic trees, the lower 2/3 - 3/4 of the molecular layer (Palay and Chan-Palay, 1974), and parallel fibers synapse on more distal regions. If spine density varies along the dendritic tree, this could provide important information about the type of input and fiber at a particular location. Overall, the results of this investigation provide a greater understanding of the dendritic spine density in the normal Purkinje cell and provide a basis for future comparison of spine density in subjects with neurological disorders, mental retardation, and physiological conditions.

An adaptation of the text and figures from Chapters 1, 2, 3, and 4 will be submitted for publication with the following co-authors: Eric Bushong, Maryann Martone, Mark Ellisman, Naoko Yamada, Andrea Thor, Erik De Schutter, and Masako Terada. The thesis author was the primary contributor to the work of this chapter.

REFERENCES

Bailey CH, Bartsch D, Kandel ER. 1996. Toward a molecular definition of long-term memory storage. Proc Natl Acad Sci U S A 93:13445-52

Bailey CH, Kandel ER. 1993. Structural changes accompanying memory storage. Annu Rev Physiol 55:397-426

Baumeister W. 2005. From proteomic inventory to architecture. FEBS Lett 579:933-7

Belichenko PV, Krasnov IB. 1991. The dendritic spines of the pyramidal neurons in layer V of the rat sensorimotor cortex following a 14-day space flight. Biull Eksp Biol Med 112:541-2

Benitez-Bribiesca L, De la Rosa-Alvarez I, Mansilla-Olivares A. 1999. Dendritic spine pathology in infants with severe protein-calorie malnutrition. Pediatrics 104:e21

Bennett PM. 1974. Decrease in section thickness on exposure to the electron beam; the use of tilted sections in estimating the amount of shrinkage. J Cell Sci 15:693-701

Bhatt DH, Zhang S, Gan WB. 2009. Dendritic spine dynamics. Annu Rev Physiol 71:261-82

Blomberg F, Cohen RS, Siekevitz P. 1977. The structure of postsynaptic densities isolated from dog cerebral cortex. II. Characterization and arrangement of some of the major proteins within the structure. J Cell Biol 74:204-25

Braitenberg V, Atwood RP. 1958. Morphological observations on the cerebellar cortex. J Comp Neurol 109:1-33

Chedotal A, Sotelo C. 1992. Early Development of Olivocerebellar Projections in the Fetal Rat Using CGRP Immunocytochemistry. Eur J Neurosci 4:1159-79

Chen Y, Dube CM, Rice CJ, Baram TZ. 2008. Rapid loss of dendritic spines after stress involves derangement of spine dynamics by corticotropin-releasing hormone. J Neurosci 28:2903-11

Chow SK, Hakozaki H, Price DL, MacLean NA, Deerinck TJ. 2006. Automated microscopy system for mosaic acquisition and processing. J Microsc 222:76-84

Connor JR, Diamond MC. 1982. A comparison of dendritic spine number and type on pyramidal neurons of the visual cortex of old adult rats from social or isolated environments. J Comp Neurol 210:99-106

Crick F. 1982. Do dendritic spines twitch? Trends in Neurosciences 5:44-6

DeFelipe J. 2006. Brain plasticity and mental processes: Cajal again. Nat Rev Neurosci 7:811-7

Demoor J. 1896. La plasticité morphologique des neurones cérébraux. Arch Biol (Bruxelles) 14:723-51

Denk W, Horstmann H. 2004. Serial block-face scanning electron microscopy to reconstruct three-dimensional tissue nanostructure. PLoS Biol 2:e329

Desmond NL, Levy WB. 1983. Synaptic correlates of associative potentiation/depression: an ultrastructural study in the hippocampus. Brain Res 265:21-30

Dunaevsky A, Tashiro A, Majewska A, Mason C, Yuste R. 1999. Developmental regulation of spine motility in the mammalian central nervous system. Proc Natl Acad Sci U S A 96:13438-43

Engert F, Bonhoeffer T. 1999. Dendritic spine changes associated with hippocampal long-term synaptic plasticity. Nature 399:66-70

Feldman ML, Dowd C. 1975. Loss of dendritic spines in aging cerebral cortex. Anat Embryol (Berl) 148:279-301

Ferrer I, Gullotta F. 1990. Down's syndrome and Alzheimer's disease: dendritic spine counts in the hippocampus. Acta Neuropathol 79:680-5

Fifkova E, Delay RJ. 1982. Cytoplasmic actin in neuronal processes as a possible mediator of synaptic plasticity. J Cell Biol 95:345-50

Fox CA, Barnard JW. 1957. A quantitative study of the Purkinje cell dendritic branchlets and their relationship to afferent fibres. J Anat 91:299-313

Fox CA, Hillman DE, Siegesmund KA, Dutta CR. 1967. The primate cerebellar cortex: a Golgi and electron microscopic study. Prog Brain Res 25:174-225

Fox CA SK, Dutta CR 1964. The Purkinje cell dendritic branchlets and their relation with the parallel fibers: light and electron microscopic observations. In: Cohen M, Snider RS (eds) Morphological and biochemical correlates of neural activity. pp. 112-41. New York: Harper and Row

Frey TG, Perkins GA, Ellisman MH. 2006. Electron tomography of membrane-bound cellular organelles. Annu Rev Biophys Biomol Struct 35:199-224

Gray EG. 1959. Axo-somatic and axo-dendritic synapses of the cerebral cortex: an electron microscope study. J Anat 93:420-33

Gray EG. 1959. Electron microscopy of synaptic contacts on dendrite spines of the cerebral cortex. Nature 183:1592-3

Hamori JaS, J. 1964. The "crossing over" synapse: an electron microscopic study of the molecular layer in the cerebellar cortex. Acta Biol Acad Scie Hun 15:95-117

Harris KM, Kater SB. 1994. Dendritic spines: cellular specializations imparting both stability and flexibility to synaptic function. Annu Rev Neurosci 17:341-71

Harris KM, Stevens JK. 1988a. Dendritic spines of rat cerebellar Purkinje cells: serial electron microscopy with reference to their biophysical characteristics. J Neurosci 8:4455-69

Harris KM, Stevens, JK. 1988b. Study of dendritic spines by serial electron microscopy and three-dimensional reconstructions. In Neurology and Neurobiology pp. 179-99. New York: Alan R. Liss

Heinsen H, Heinsen YL. 1983. Quantitative studies on regional differences in Purkinje cell dendritic spines and parallel fiber synaptic density. Anat Embryol (Berl) 168:361-70

Hillman DE, Chen S. 1984. Reciprocal relationship between size of postsynaptic densities and their number: constancy in contact area. Brain Res 295:325-43

Hinton VJ, Brown WT, Wisniewski K, Rudelli RD. 1991. Analysis of neocortex in three males with the fragile X syndrome. Am J Med Genet 41:289-94

Irwin SA, Patel B, Idupulapati M, Harris JB, Crisostomo RA. 2001. Abnormal dendritic spine characteristics in the temporal and visual cortices of patients with fragile-X syndrome: a quantitative examination. Am J Med Genet 98:161-7

Isokawa M. 2000. Remodeling dendritic spines of dentate granule cells in temporal lobe epilepsy patients and the rat pilocarpine model. Epilepsia 41 Suppl 6:S14-7

Kremer JR, Mastronarde DN, McIntosh JR. 1996. Computer visualization of three-dimensional image data using IMOD. J Struct Biol 116:71-6

Lee KJ, Jung JG, Arii T, Imoto K, Rhyu IJ. 2007. Morphological changes in dendritic spines of Purkinje cells associated with motor learning. Neurobiol Learn Mem 88:445-50

Li C, Brake WG, Romeo RD, Dunlop JC, Gordon M. 2004. Estrogen alters hippocampal dendritic spine shape and enhances synaptic protein immunoreactivity and spatial memory in female mice. Proc Natl Acad Sci U S A 101:2185-90

Lowndes M, Stewart MG. 1994. Dendritic spine density in the lobus parolfactorius of the domestic chick is increased 24 h after one-trial passive avoidance training. Brain Res 654:129-36

M.E. Martone TJD, N. Yamada, E. Bushong and M.H. Ellisman. 2000. Correlated 3D light and electron microscopy: use of high voltage microscopy tomography for imaging large biological structures. J. Histotechnol 23:261-70

Marin-Padilla M. 1976. Pyramidal cell abnormalities in the motor cortex of a child with Down's syndrome. A Golgi study. J Comp Neurol 167:63-81

Matus A, Ackermann M, Pehling G, Byers HR, Fujiwara K. 1982. High actin concentrations in brain dendritic spines and postsynaptic densities. Proc Natl Acad Sci U S A 79:7590-4

Morrison ME, Mason CA. 1998. Granule neuron regulation of Purkinje cell development: striking a balance between neurotrophin and glutamate signaling. J Neurosci 18:3563-73

Moser MB, Trommald M, Andersen P. 1994. An increase in dendritic spine density on hippocampal CA1 pyramidal cells following spatial learning in adult rats suggests the formation of new synapses. Proc Natl Acad Sci U S A 91:12673-5

Napper RM, Harvey RJ. 1988a. Number of parallel fiber synapses on an individual Purkinje cell in the cerebellum of the rat. J Comp Neurol 274:168-77

Napper RM, Harvey RJ. 1988b. Quantitative study of the Purkinje cell dendritic spines in the rat cerebellum. J Comp Neurol 274:158-67

Nimchinsky EA, Sabatini BL, Svoboda K. 2002. Structure and function of dendritic spines. Annu Rev Physiol 64:313-53

Norrholm SD, Bibb JA, Nestler EJ, Ouimet CC, Taylor JR, Greengard P. 2003. Cocaine-induced proliferation of dendritic spines in nucleus accumbens is dependent on the activity of cyclin-dependent kinase-5. Neuroscience 116:19-22

Palay SL, Chan-Palay V. 1974. Cerebellar cortex: cytology and organization. Berlin, Heidelberg, New York,: Springer. xii, 348 p. pp.

Perkins GA, Renken CW, Song JY, Frey TG, Young SJ. 1997. Electron tomography of large, multicomponent biological structures. J Struct Biol 120:219-27

Petit TL, LeBoutillier JC. 1979. Effects of lead exposure during development on neocortical dendritic and synaptic structure. Exp Neurol 64:482-92

Purpura DP. 1975. Dendritic differentiation in human cerebral cortex: normal and aberrant developmental patterns. Adv Neurol 12:91-134

Pysh JJ, Weiss GM. 1979. Exercise during development induces an increase in Purkinje cell dendritic tree size. Science 206:230-2

Robinson TE, Gorny G, Mitton E, Kolb B. 2001. Cocaine self-administration alters the morphology of dendrites and dendritic spines in the nucleus accumbens and neocortex. Synapse 39:257-66

Robinson TE, Kolb B. 1999. Alterations in the morphology of dendrites and dendritic spines in the nucleus accumbens and prefrontal cortex following repeated treatment with amphetamine or cocaine. Eur J Neurosci 11:1598-604

Rollenhagen A, Bischof HJ. 1991. Rearing conditions affect neuron morphology in a telencephalic area of the zebra finch. Neuroreport 2:711-4

Rosenzweig MR, Bennett EL. 1996. Psychobiology of plasticity: effects of training and experience on brain and behavior. Behav Brain Res 78:57-65

Roth A, Hausser M. 2001. Compartmental models of rat cerebellar Purkinje cells based on simultaneous somatic and dendritic patch-clamp recordings. J Physiol 535:445-72

Santamaria F, Wils S, De Schutter E, Augustine GJ. 2006. Anomalous diffusion in Purkinje cell dendrites caused by spines. Neuron 52:635-48

Segal I, Korkotian I, Murphy DD. 2000. Dendritic spine formation and pruning: common cellular mechanisms? Trends Neurosci 23:53-7

Shors TJ, Chua C, Falduto J. 2001. Sex differences and opposite effects of stress on dendritic spine density in the male versus female hippocampus. J Neurosci 21:6292-7

Spacek J, Hartmann M. 1983. Three-dimensional analysis of dendritic spines. I. Quantitative observations related to dendritic spine and synaptic morphology in cerebral and cerebellar cortices. Anat Embryol (Berl) 167:289-310

Stefanowska M. 1897a. Les appendices terminaux des dendrites cerebraux et leur differents etats physiologiques. Arch. Sei. Phys., Geneve, 11, 1901, (488-511, mit l Taf.). [1270 4560 1290]. 2534. Ann. Soc. R. Sci. Med. Nat. Brux. 6:351–407

Stefanowska M. 1897a. Sur les appendices des dendrites. Bull. Soc. R. Sci. Med. Nat. Brux 55:76–81

Takashima S, Becker LE, Armstrong DL, Chan F. 1981. Abnormal neuronal development in the visual cortex of the human fetus and infant with down's syndrome. A quantitative and qualitative Golgi study. Brain Res 225:1-21

Takashima S, Iida K, Mito T, Arima M. 1994. Dendritic and histochemical development and ageing in patients with Down's syndrome. J Intellect Disabil Res 38 (Pt 3):265-73

Tavares MA, Paula-Barbosa MM, Gray EG. 1983. A morphometric Golgi analysis of the Purkinje cell dendritic tree after long-term alcohol consumption in the adult rat. J Neurocytol 12:939-48

Vecellio M, Schwaller B, Meyer M, Hunziker W, Celio MR. 2000. Alterations in Purkinje cell spines of calbindin D-28 k and parvalbumin knock-out mice. Eur J Neurosci 12:945-54

Weiss GM, Pysh JJ. 1978. Evidence for loss of Purkinje cell dendrites during late development: a morphometric Golgi analysis in the mouse. Brain Res 154:219-30

Willis RA. 1973. Optimization of stereoscopic and high angle tilting procedures for biological thin sections. J Microsc 98:379-95

Wiseman PW, Capani F, Squier JA, Martone ME. 2002. Counting dendritic spines in brain tissue slices by image correlation spectroscopy analysis. J Microsc 205:177-86

Wisniewski KE, Segan SM, Miezejeski CM, Sersen EA, Rudelli RD. 1991. The Fra(X) syndrome: neurological, electrophysiological, and neuropathological abnormalities. Am J Med Genet 38:476-80

Yuste R, Bonhoeffer T. 2001. Morphological changes in dendritic spines associated with long-term synaptic plasticity. Annu Rev Neurosci 24:1071-89

Yuste R, Bonhoeffer T. 2004. Genesis of dendritic spines: insights from ultrastructural and imaging studies. Nat Rev Neurosci 5:24-34

Zito K, Murthy VN. 2002. Dendritic spines. Curr Biol 12:R5